A Comprehensive Literature Review of SAR Polarimetric Calibration for the Waseda SAR Sensor

Prepared by:

Abdullah Algafsh

ALGABD001

Department of Electrical Engineering
University of Cape Town

Prepared for:

Professor Michael Inggs

Department of Electrical Engineering

Department of Electrical Engineering
University of Cape Town

April 2015

Submitted to the Department of Electrical Engineering at the University of Cape Town in partial fulfilment of the academic requirements for a

Master of Science in Electrical Engineering

Declaration

1. **I know that plagiarism is wrong. Plagiarism is to use another's work and pretend that it is one's own.**
2. **I have used the IEEE convention for citation and referencing. Each contribution to, and quotation in, this project report from the work(s) of other people, has been attributed and has been cited and referenced.**
3. **This project report is my own work.**
4. **I have not allowed, and will not allow, anyone to copy my work with the intention of passing it off as their own work or part thereof**

Name: **Abdullah Algafsh**

Signature:

Date: 29 April 2015

Acknowledgments

Firstly, I would like to thank my supervisor Prof. Michael Inggs from the department of Electrical Engineering for his guidance and help throughout my dissertation.

I want to thank my family for their support during my masters' degree studies in Cape Town. I would like also to extend my thanks to my wife Hessah and my daughter Hla who have been with me through the whole journey.

Finally, I would like to express my deepest thanks to all who contributed towards my dissertation.

Abstract

This dissertation deals with a comprehensive literature review on SAR polarimetric calibration, as well as developing a polarimetric calibration procedure to be used for calibrating the sensor for the Waseda SAR project. The complete work is presented in six chapters. The dissertation starts by introducing Synthetic Aperture Radar Polarimetry (SAR polarimetry) by identifying the research objectives, and explains Waseda SAR project between King Abdulaziz City for Science and Technology and the University of Cape Town.

A comprehensive literature review on SAR polarimetric calibration is introduced in the dissertation. The literature review explains the developments in calibration methods from the early 1960's to recent years, including passive and active reflector advantages as well as the limitations for both reflectors. Also, displaying the received power as a function of polarization in a graphic way is presented in the dissertation known as the 'polarization signature'. Two examples are used which are: the trihedral corner reflector and the dihedral corner reflector. The two examples are the theoretical reference for the calibration procedure for Waseda SAR sensor.

The calibrated data set collected from NASA's Uninhabited Aerial Vehicle Synthetic Aperture Radar (UAVSAR) over California is analyzed. The data is contaminated with an unrealistically high amount of coupling (-5 dB) to show the coupling effect on the data and then remove the amount of coupling to return the data to its original form.

The dissertation concludes with a calibration procedure to be used for calibrating Waseda SAR sensor using the presented methods of SAR polarimetric calibration. The procedure involves using external devices such as: trihedral corner reflectors and dihedral corner reflectors as well as calculating the sizes of the reflectors and how the calibration flights are to be coordinated and instrumented with the reflectors.

Contents

Contents

List of Figures

List of Figures

List of Tables

List of Acronyms

SAR	Synthetic Aperture Radar
KACST	King Abdulaziz city for science and technology
UCT	University of Cape Town
EM	Electro Magnetic
RCS	Radar Cross Section
IDL	Interactive Data Language
ENVI	Exelis Visual Information Solutions
ARC	Active Radar Calibrator
DEM	Digital Elevation Model

1

Introduction

1.1. Introduction

Synthetic Aperture Radar (SAR) was developed in the 1950's. It was developed for long-range mapping from an aerial view which includes views from space. They have since been developed into better performing sensors with capabilities such as: multi-polarization data gathering, wide-swath coverage, and multi-frequency radar imaging [1].

One of the on-going developments in the field of remote sensing is synthetic aperture radar polarimetry. It has become an important tool to monitor the earth because of it is ability to provide information about the physical properties of the surface. This document will provide a comprehensive literature review on the development of synthetic aperture radar polarimetry as well as developing a polarimetric calibration procedure which can be implemented in the Waseda SAR sensor for the project between KACST (King Abdulaziz City for Science and Technology) and UCT (University of Cape Town).

This chapter will introduce the research objective and Waseda SAR project between KACST and UCT in detail with all the requirements for the s. The second chapter is a review on SAR polarimetry with a mathematical representation of all the matrices and equations. Also, synthetic aperture radar polarimetry decomposition will be introduced in the chapter to extract reliable information from the backscatter. The section will introduce various coherent and incoherent target decomposition methods and provide a comparison between them.

The third chapter is a comprehensive literature review on the calibration of SAR polarimetry. The chapter is divided into two sections. The first section will introduce passive corner reflectors and focus on two passive reflectors which are the trihedral and the dihedral corner reflectors with their specifications. Also, the section will introduce active calibration to show the design, and explain how active calibration can be done, as well as its major advantages over passive reflectors. Finally, the last part in section one will be on three general calibration process for polarimetric radar image data which are: cross talk estimated and corrected, co-polarized channel phase imbalance calibration, and absolute radiometric calibration. The second section in chapter three introduces the phenomena of the polarization signature which is also known as a polarization response. A polarization signature is the process of displaying the received power as a function of polarization in a graphic way. In this section, two examples of polarization signatures will be introduced with their equations for power and the matrices. The first example is the trihedral corner reflector which will be used many times in our calibration. The second example is the dihedral corner reflector which will also be used in our calibration procedure, especially in overall calibration process.

Chapter four in the dissertation analyzes data that was obtained from the UAVSAR (Uninhabited Aerial Vehicle Synthetic Aperture Radar) and that is available for download from Jet Propulsion Laboratory (JPL). UAVSAR is a NASA L-band SAR system. The data was collected in southern California and is calibrated. The objective of analyzing the data is to contaminate the calibrated data with an unrealistically high amount of coupling (-5 dB) between HH (horizontal transmit and horizontal receive) and VV (vertical transmit and vertical receive) as well as between HV (horizontal transmit and vertical receive) and both HH, VV. After contaminating the data, the images are produced to show the coupling between these channels. Finally, we will pick up one pixel on the image to show the difference between the pure pixel and the contaminated one, and represent them in a vector format.

The fifth chapter summarizes all the theories and methods which were explained in the previous chapters, to come up with an appropriate way of calibrating Waseda. The first part of the chapter explains the overall structure of the calibration process, to give an idea of how the data will be calibrated, then the method and areas of collecting the data using our SAR system. The third part is a detailed polarimetric calibration procedure which involves three steps that will be used for calibrating the Waseda SAR sensor. Finally, the use of external corner reflectors for Waseda is presented as well as calculating the sizes of the reflectors and how the calibration flights are to be coordinated and instrumented with the reflectors.

The dissertation wraps up with chapter six giving a summary of the results, as well as additional work and recommendations to be implemented in the future.

1.2. Research Objectives

The main objective of this dissertation is to provide a comprehensive literature review on SAR polarimetric calibration and to develop a polarimetric calibration procedure to be used for calibrating the sensor for the Waseda SAR project between UCT and KACST.

1.3. Waseda Project

A three year project between KACST (King Abdulaziz City for Science and Technology) and UCT (University of Cape Town) started in 2014. The main objective of the project is to use SAR technology to detect red weevil infested palm trees which came from the tropical regions of Asia, and are a serious problem in Saudi Arabia [2]. Two bands will be used in Waseda SAR system which are X and P. Figure 1.1 gives an idea of the use of these two different bands. The P-band has a longer wavelength and penetrates through vegetation thereby maximising backscatter from the terrain surface rather than vegetation components. One the other hand, the X-band has a shorter wavelength which leads to backscattering from the canopy of vegetation.

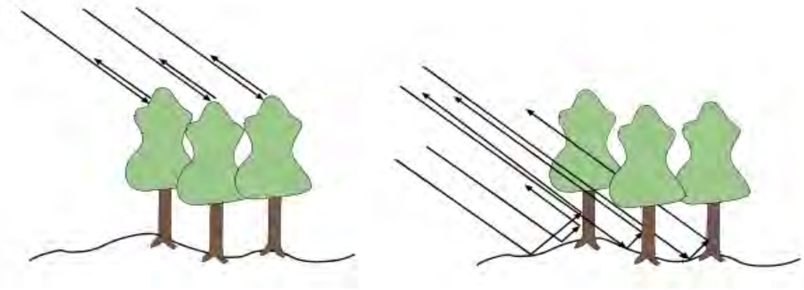

Figure 1.1: Penetration dependency frequencies for X-band left image and P-band right image [3]**.**

The two sensors will be fitted to an aircraft such as the **Cessna 208** to collect data. Table 1.1 below shows the specifications for the two sensors.

Table 1.1: System specification for Waseda SAR sensor

	X band	***P band***
Frequency	*9.6 GHz*	*500 MHz*
Bandwidth	*up to 500 MHz*	*up to 200 MHz*
4 Tx channel	*2 X band*	*2 P band*
4 Rx channel	*2 X band*	*2 P band*
Polarimetric Antenna	*40 degrees in elevation* *5 in azimuth* *25 dB polarimetric isolation*	*60 degrees in elevation,* *60 degrees in azimuth* *25 dB polarimetric isolation*

The X and P band antenna will be built by MetaSensing, which is an innovative Dutch remote sensing company, founded by Italian scientist and engineer Adriano Meta in 2008 with the aim of commercializing the new compact, high resolution radar mapping technology. The two sensors will be delivered in mid-2016 to be installed in an aircraft to collect the data. The system is monostatic and a full polarimetric SAR system. The calibration procedure for the system will follow the exact procedure which is developed in this dissertation and the data will be collected in Saudi Arabia and other locations depending on availability and the aviation costs.

The following chapter will provide a basic knowledge of Synthetic Aperture Radar (SAR) with a mathematical representation of all the matrices and equations. Also, Synthetic Aperture Radar Polarimetry decomposition will be introduced to extract the reliable information from the backscatter with two coherent and incoherent target decomposition methods and a comparison between them.

2

SAR Polarimetry

2.1. SAR Polarimetry

In general, SAR Polarimetry can be defined as the science of acquiring, processing and analyzing the polarization state of an electromagnetic field [4]. Polarimetric SAR has the capacity to separate the various scattering elements available in a single SAR resolution cell. SAR polarimetry deals with information retrieval using the polarization properties of electromagnetic waves. The following figure shows the propagation of an electromagnetic wave.

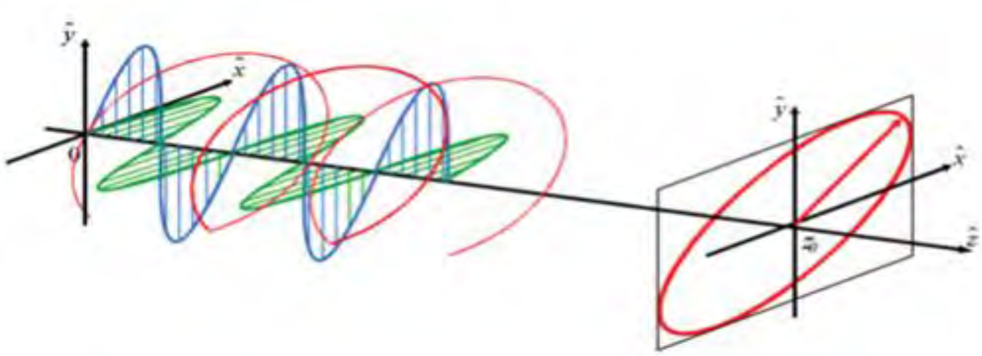

Figure 2.1: Propagation of an Electromagnetic plan wave [5]**.**

Figure 2.1 shows the polarization of an electromagnetic field. The horizontal electric field is represented on the x-axis, and the vertical electric field on the y-axis. They are combined to form the net electric field. Additionally, the combination of the horizontal and vertical fields is going to create an ellipse known as a polarization ellipse [5].

Before moving to the polarization ellipse, there are things that need to be described, defined, and be cleared up, such as: the polarization categories, four combinations of transmitting and receiving polarizations, and the levels of polarization complexity.

There are three categories of polarization shown in figure 2.2 which are: linear, circular, and elliptical polarization. The linear polarization occurs by broadcasting the EM wave in either vertical or horizontal directions while circular polarization occurs by broadcasting the EM wave on two planes, making one complete revolution in a single wavelength. The last category is elliptical polarization, which occurs when there is a mix of linear and circular polarization. Figure 2.2 below shows the three different types of polarization categories.

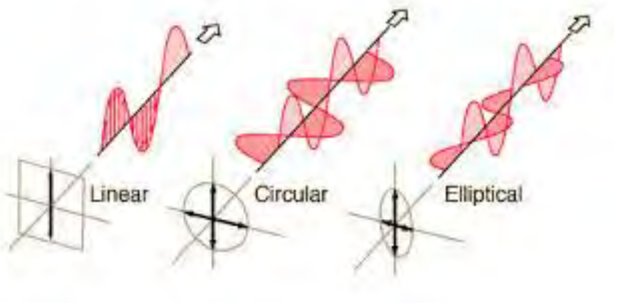

Figure 2.2: Categories of polarization: linear, circular, and elliptical [6]

A radar system has the following channels using H and V linear polarizations [7]:

- HH - for horizontal transmit and horizontal receive, (**HH**)
- VV - for vertical transmit and vertical receive, (**VV**)
- HV - for horizontal transmit and vertical receive (**HV**)
- VH - for vertical transmit and horizontal receive (**VH**)

The first two polarization combinations are co-polarized because they have the same transmit, and receive polarizations; while the last two combinations are cross-polarized because transmit and receive polarizations are orthogonal to one another.

A radar system has different polarization complexity levels [7]:

- Single polarized - HH or VV or HV or VH
- Dual polarized - HH and HV, VV and VH, or HH and VV
- Quad polarizations - HH, VV, HV, and VH.

2.1.1. Polarization Ellipse

The electric field vector of a fully polarized wave traces out a regular pattern, when visualized along the direction of propagation of the wave, which is generally an ellipse known as a polarization ellipse, shown in the figure 2.3 below.

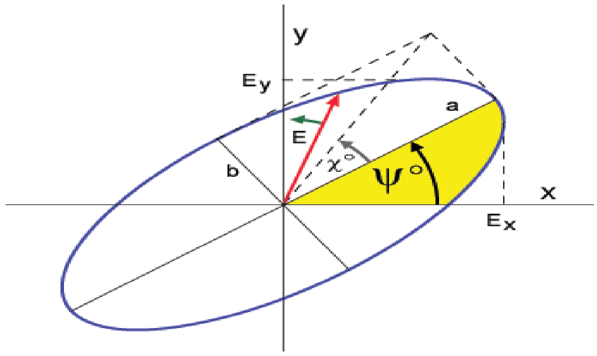

Figure 2.3: Polarization Ellipse [8]

As shown in figure 2.3, the amplitude of a received horizontal component represented by E_x and the amplitude of a received vertical component is represented by E_y. By combining the two, we can find the polarization ellipse. The ellipse has two axes: one is a semi-major axis of length a, and the other is a semi-minor axis of length b, with an angle measured counter-clockwise from the positive horizontal axis. The angle is called the orientation angle Ψ, which has a value between 0° and 180°. Moreover, the degree to which the ellipse is oval, is described by a shape parameter called ellipticity, defined as χ = arctan(b/a), and has a values from -45° to +45°. The magnitude and the phase between the horizontal and vertical components of the electric field vector, control the shape of the ellipse. [9]

The scientist, Gabriel Stokes, came up with the Stokes vector which is identified by four elements $[S_0 \; S_1 \; S_2 \; S_3]^T$, to describe the polarization state of electromagnetic wave. [10]

$$\begin{bmatrix} S_0 \\ S_1 \\ S_2 \\ S_3 \end{bmatrix} = \begin{bmatrix} |E_y|^2 + |E_x|^2 \\ |E_y|^2 - |E_x|^2 \\ 2\,Re\,\{E_y {E_x}^*\} \\ 2\,Im\,\{E_y {E_x}^*\} \end{bmatrix} = \begin{bmatrix} \mathrm{S}_0 \\ \mathrm{S}_0 \cos 2\,\Psi \cos 2\chi \\ \mathrm{S}_0 \sin 2\,\Psi \cos 2\chi \\ \mathrm{S}_0 \sin 2\chi \end{bmatrix}. \qquad (2.1)$$

where |.| is the absolute value and * is the complex conjugate. Also, the first parameter S_0 is the total power of an EM wave and derived from the return of the amplitude E_x and E_y. The second parameter S_1 represents the difference between the density powers related to the horizontal and vertical polarizations, and the last two parameters S_2 and S_3 represent the phase difference between the horizontal and vertical components of the electric field. This formalism describe the polarization state of electromagnetic wave by orientation, ellipticity, and the parameter S_0. On the other hand, the EM wave can be completely polarized, completely un-polarized, or partially polarized. In the completely polarized case, only three parameters out of the four are independent and its total power is represented as:

$$S_0^2 = {\mathrm{S}_1}^2 + {\mathrm{S}_2}^2 + {\mathrm{S}_3}^2 \qquad (2.2)$$

On the other hand, completely un-polarized has an equal magnitude E_x and E_y, and a random phase angle. In the partially polarized wave, it means that the sum of the two waves is completely polarized, and un-polarized. The total power is greater than the polarized power.

Finally, wave polarization can be represented in degrees of polarization, where it is 1 for completely polarized, and 0 for completely un-polarized. [9]

$$\text{Degree of polarization} = \frac{\sqrt{S_1{}^2+S_2{}^2+S_3{}^2}}{S_0} \tag{2.3}$$

2.1.2. Scattering Matrix

After introducing the representation of electromagnetic waves, the scattering of the polarization from a target will be presented. In the scattering matrix, all the possible polarimetric linear components will be used. The scattering matrix is a 2×2 matrix, which consists of four complex elements. As shown below, the co-polarized information is represented in the diagonal elements, while the cross-polarized information is represented in the off-diagonal elements.

$$\mathrm{S} = \begin{bmatrix} S_{HH} & S_{HV} \\ S_{VH} & S_{VV} \end{bmatrix} \tag{2.4}$$

By using the scattering matrix elements, it is not directly possible to extract the different type of the received data. So, we are going to alter the basis, by decomposing the scattering to extract the varying types of scattering information retrieval. So, from the scattering matrix, two feature vectors will be generated, which are the lexicographical feature vector and the Pauli feature vector and will be explained in the following two points:

2.1.2.1. Lexicographical feature vector

Lexicographical feature vector [11] is obtained from the simple lexicographical expansion of scattering matrix [S], using a lexicographic basis [Ψ_L]. As shown below, the matrix of the lexicographic contains four matrices. The first matrix to the left only considers the first element which is S_{HH} and the remainders are zeros. The second matrix only considers the second element and the remainders are zeros, and similarly, the third and the fourth matrices.

$$[\Psi_L] = \left\{2\begin{bmatrix} 1 & 0 \\ 0 & 0 \end{bmatrix} 2\begin{bmatrix} 0 & 1 \\ 0 & 0 \end{bmatrix} \; 2\begin{bmatrix} 0 & 0 \\ 1 & 0 \end{bmatrix} \; 2\begin{bmatrix} 0 & 0 \\ 0 & 1 \end{bmatrix}\right\} \tag{2.5}$$

Finally, by combining these elements we get one matrix known as a lexicographical feature vector.

$$F_L = [S_{HH} \quad S_{HV} \quad S_{VH} \quad S_{VV}] \tag{2.6}$$

2.1.2.2. Pauli feature vector

A Pauli feature vector is obtained from the renowned complex Pauli spin basis set [Ψ_P]. As shown below, the Pauli basis set has four matrices. The first matrix to the left, only considers the diagonal elements, which are S_{HH} and S_{VV}, and we will obtain the sum of the diagonal elements. The second matrix is contrary, as one of the diagonal elements is negative, so we will have S_{HH} minus S_{VV}. [11]

$$[\Psi_P] = \left\{\sqrt{2}\begin{bmatrix}1 & 0\\0 & 1\end{bmatrix} \sqrt{2}\begin{bmatrix}1 & 0\\0 & -1\end{bmatrix} \sqrt{2}\begin{bmatrix}0 & 1\\1 & 0\end{bmatrix} \sqrt{2}\begin{bmatrix}0 & -j\\j & 0\end{bmatrix}\right\} \tag{2.7}$$

Finally, we will come up with the following Pauli feature vector

$$f_{4p} = [f_0 \quad f_1 \quad f_2 \quad f_3]_P^T$$

$$f_{4p} = \frac{1}{\sqrt{2}}[S_{HH} + S_{VV} \quad S_{VV} - S_{HH} \quad S_{HV} + S_{VH} \quad j(S_{HV} - S_{VH})]^T \tag{2.8}$$

If we want to correlate the Pauli basis and the scattering matrix, then it may be represented in terms of a Pauli feature vector as follows:

$$[S]_P = \frac{1}{\sqrt{2}}\begin{bmatrix}f_0 - f_1 & f_2 - jf_3\\f_2 + jf_1 & f_0 + f_1\end{bmatrix} = [S] \tag{2.9}$$

However, the information which is provided by the scattering matrix is insufficient to describe the physical properties of the surface. Two approaches are used to express target proprieties, which are: a covariance matrix and a coherency matrix, and are explained as follows:

2.1.3. Covariance matrix

A covariance matrix is generated on the basis of a lexicographical feature vector. As shown below, the 4×4 lexicographic a polarimetric covariance matrix is generated using a product of a feature vector with its conjugate.

$$\mathrm{K_L} = \begin{bmatrix} \mathrm{S_{HH}} \\ \mathrm{S_{HV}} \\ \mathrm{S_{VH}} \\ \mathrm{S_{VV}} \end{bmatrix} = [\mathrm{S_{HH}} \quad \mathrm{S_{HV}} \quad \mathrm{S_{VH}} \quad \mathrm{S_{VV}}]^{\mathrm{T}} \tag{2.10}$$

$$\mathrm{C_L} = \mathrm{K_L^* K_L^{+}} = \begin{bmatrix} < |\mathrm{S_{HH}}|^2 > & < \mathrm{S_{HH}S_{HV}^*} > & < \mathrm{S_{HH}S_{VH}^*} > & < \mathrm{S_{HH}S_{VV}^*} > \\ < \mathrm{S_{HV}S_{HH}^*} > & < |\mathrm{S_{HV}}|^2 > & < \mathrm{S_{HV}S_{VH}^*} > & < \mathrm{S_{HV}S_{VV}^*} > \\ < \mathrm{S_{VH}S_{HH}^*} > & < \mathrm{S_{VH}S_{HV}^*} > & < |\mathrm{S_{VH}}|^2 > & < \mathrm{S_{VH}S_{VV}^*} > \\ < \mathrm{S_{VV}S_{HH}^*} > & < \mathrm{S_{VV}S_{HV}^*} > & < \mathrm{S_{VV}S_{VH}^*} > & < |\mathrm{S_{VV}}|^2 > \end{bmatrix} \tag{2.11}$$

In a similar way, the coherency matrix can be generated from a Pauli feature vector, and represented by 4×4 coherency matrix as follows:

$$[\mathrm{T}] = \mathrm{K_P K_P^*} \tag{2.12}$$

In the case of a monostatic SAR system, where it follows the reciprocity assumption, the assumption is that the information which is carried by cross-polarized channels is the same. That means: $S_{HV} = S_{VH}$. As shown below, there is no need to use both VH and HV, so we are going to use one of them, as they are the same and the lexicographical feature vector matrix will be 3×1 as follows: [12]

$$\mathrm{K_L} = \begin{bmatrix} \mathrm{S_{HH}} \\ \sqrt{2}\mathrm{S_{HV}} \\ \mathrm{S_{VV}} \end{bmatrix} \tag{2.13}$$

Finally, the 9 elements of covariance matrix can be written as:

$$[\mathrm{C}] = \mathrm{K_L K_L^*} = \begin{bmatrix} \mathrm{S_{HH}S_{HH}^*} & \sqrt{2}\mathrm{S_{HH}S_{HV}^*} & \mathrm{S_{HH}S_{VV}^*} \\ \sqrt{2}\mathrm{S_{HV}S_{HH}^*} & 2\mathrm{S_{HV}S_{HV}^*} & \sqrt{2}\mathrm{S_{HV}S_{VV}^*} \\ \mathrm{S_{VV}S_{HH}^*} & \sqrt{2}\mathrm{S_{VV}S_{HV}^*} & \mathrm{S_{VV}S_{VV}^*} \end{bmatrix}. \tag{2.14}$$

where * represents the complex conjugate.

Another case is reflection symmetry, where co-polarized and cross polarized backscatter are not correlated. A covariance matrix will show a zero value for off diagonal elements as follows: [12]

$$[\mathrm{C}] = K_L K_L^* = \begin{bmatrix} S_{HH}S_{HH}^* & 0 & S_{HH}S_{VV}^* \\ 0 & 2S_{HV}S_{HV}^* & 0 \\ S_{VV}S_{HH}^* & 0 & S_{VV}S_{VV}^* \end{bmatrix}. \tag{2.15}$$

where * represents the complex conjugate.

2.1.4. Coherency matrix

A coherency matrix is generated on the basis of a Pauli feature vector, and by following the reciprocity assumption again below, the Pauli feature vector for the fourth element, $j(S_{HV}\text{-}\ S_{VH})$, is zero

$$\mathrm{K_{4p}} = [\mathrm{f_0} \quad \mathrm{f_1} \quad \mathrm{f_2} \quad \mathrm{f_3}]_{\mathrm{P}}^{\mathrm{T}}$$

$$\mathrm{K_{4p}} = \frac{1}{\sqrt{2}}[\mathrm{S_{HH}} + \mathrm{S_{VV}} \quad \mathrm{S_{VV}} \text{-}\ \mathrm{S_{HH}} \quad \mathrm{S_{HV}} + \mathrm{S_{VH}} \quad \mathrm{j(S_{HV}} \text{-}\ \mathrm{S_{VH})}]^{\mathrm{T}} \tag{2.16}$$

The Pauli matrix will be in the form of a 3×1 as follows:

$$\mathrm{K_{3P}} = \frac{1}{\sqrt{2}}\begin{bmatrix} \mathrm{S_{HH}} + \mathrm{S_{VV}} \\ \mathrm{S_{HH}} - \mathrm{S_{VV}} \\ 2\ \mathrm{S_{HV}} \end{bmatrix} \tag{2.17}$$

The coherency matrix will have the form of a 3×3 matrix which is the result of multiplying $K_P K_P^*$, and can be defined as:

$$[\mathrm{T}] = \mathrm{K_P K_P^*} =$$

$$\frac{1}{2}\begin{bmatrix} < |S_{HH}+S_{VV}|^2 > & < (S_{HH}+S_{VV})(S_{HH}-S_{VV})^* > & 2 < (S_{HH}+S_{VV})S_{HV}^* > \\ < (S_{HH}-S_{VV})(S_{HH}+S_{VV})^* > & < |S_{HH}-S_{VV}|^2 > & 2 < (S_{HH}-S_{VV})S_{HV}^* > \\ 2 < S_{HV}(S_{HH}+S_{VV})^* > & 2 < S_{HV}(S_{HH}-S_{VV})^* > & 4 < |S_{HV}|^2 > \end{bmatrix} \tag{2.18}$$

Finally, the reflection symmetry case for the coherency matrix, where co-polarized and cross polarized backscatter are not correlated for either side of the plane of incidence, will be as follows: [12]

$$[\mathrm{T}] = K_P K_P^* =$$

$$\frac{1}{2}\begin{bmatrix} < |S_{HH}+S_{VV}|^2 > & < (S_{HH}+S_{VV})(S_{HH}-S_{VV})^* > & 0 \\ < (S_{HH}-S_{VV})(S_{HH}+S_{VV})^* > & < |S_{HH}-S_{VV}|^2 > & 0 \\ 0 & 0 & 4 < |S_{HV}|^2 > \end{bmatrix} \tag{2.19}$$

2.2. Polarimetric Decomposition

Many mathematical and physical approaches have been established in the field of SAR polarimetry, to obtain information from the backscatter. The polarimetric decomposition is established to extract the physical information from the target.

Coherent target decomposition and incoherent target decomposition are the two major categories of target decomposition.

2.2.1. Coherent target decomposition

The coherent target decomposition, which deals with decomposition of the scattering matrix, characterizes completely polarized scatterers. Three types of coherent decomposition theorems will be presented which are: Pauli decomposition, SDH decomposition, and Cameron decomposition. [13]

2.2.1.1. Pauli decomposition

The Pauli decomposition is the most applied coherent decomposition. By considering the case of reciprocity for monostatic system ($S_{hv}= S_{vh}$) and from the Pauli basis, the scattering matrix is presented as: [13]

$$[S] = \alpha \begin{bmatrix} 1 & 0 \\ 0 & 1 \end{bmatrix} + \beta \begin{bmatrix} 1 & 0 \\ 0 & -1 \end{bmatrix} + \gamma \begin{bmatrix} 0 & 1 \\ 1 & 0 \end{bmatrix}. \qquad (2.20)$$

where

$\alpha = (S_{hh} + S_{vv}) /\sqrt{2}$

$\beta = (S_{hh} - S_{vv}) /\sqrt{2}$

$\gamma = \sqrt{2} S_{hv}$

The first matrix refers to single or odd-bounce scattering of a sphere, a plate or a trihedral. The second refers to scattering mechanisms of a dihedral, oriented at 0 degrees (double-bounce or even-bounce). The last matrix refers to a scattering mechanism of a diplane, oriented at 45 degrees.

2.2.1.2. SDH decomposition

The coherent decomposition method, formulated by Krogager [14], is based on the decomposition of any complex, symmetric scattering matrix into three components, which are: a sphere, a diplane, and right or left helix. The following formulation is presented by Krogager:

$$[S_{(h,v)}] = e^{j\varphi}\{e^{j\varphi_s} k_s [S_s] + k_d [S_d] + k_h [S_h]\} \qquad (2.21)$$

$$[S_{(h,v)}] = e^{j\varphi}\{e^{j\varphi_s} k_s \begin{bmatrix} 1 & 0 \\ 0 & 1 \end{bmatrix} + k_d \begin{bmatrix} cos2\theta & sin2\theta \\ sin2\theta & -cos2\theta \end{bmatrix} + k_h e^{\pm j2\theta} \begin{bmatrix} 1 & \pm j \\ \pm j & 1 \end{bmatrix} \}. \qquad (2.22)$$

By comparing these formulas with the previous one from the Pauli decomposition, there are six independent parameters. The parameters for Krogager decomposition are $\{\varphi.\varphi_s$, θ, k_s, k_d, $k_h\}$, where the first three are the angles, while the others are three real coefficients.

2.2.1.3. Cameron decomposition

The Cameron decomposition theorem decomposes a reciprocal target to obtain the sum of two components, which are the largest symmetric component, and minimum symmetric component. [15]

$$\vec{S} = [\cos\tau\, \vec{S}_{sym}^{max} + \sin\tau\, \vec{S}_{sym}^{min}] \tag{2.23}$$

The largest symmetric component can be presented as ($\alpha\, \vec{S}_a + \varepsilon\, \vec{S}_b$), where the α and ε are the complex entities.

2.2.2. Incoherent target decomposition

The purpose of incoherent target decomposition is to characterize distributed scatterers. It deals with the decomposition of coherency or covariance matrices. The Freeman and Yamaguchi decompositions are incoherent types of target decomposition, and will be explained as follows [13].

2.2.2.1. Freeman Decomposition

Freeman and Durden [16] presented the three component scattering mechanisms to fit in SAR polarimetric observations. The simple three scattering mechanisms of target are as follows:

Single Bounce Scattering: As shown below in figure 2.4, the first one to the left is the single bounce scattering. The single or surface bounce scattering is modeled as a first order Bragg's scattering. It is observed from the building roofs and vertical walls.

Double Bounce Scattering: As shown in the middle of figure 2.4, this type of scattering behavior is displayed by a dihedral corner reflector, such as a ground-tree trunk backscatter.

Volume Scattering: The last picture to the right in figure 2.4 represents the volume scattering mechanism, which corresponds to the multiple scattering processes occurring within a medium such as vegetation or a forest canopy.

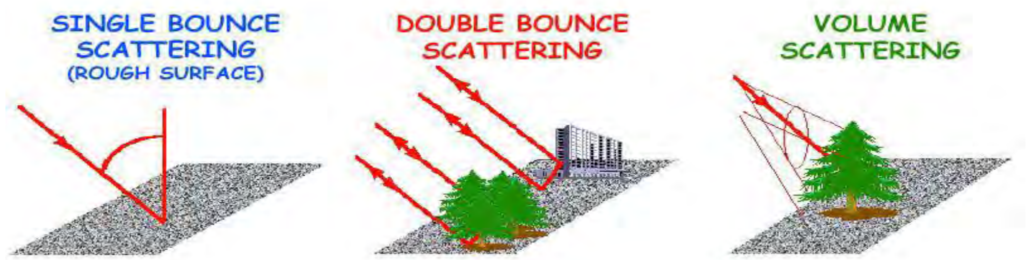

Figure 2.4: Three major scattering mechanisms [8]

The three components scattering model, which was developed by Freeman, are based on covariance matrices as follows:

$$[C] = f_s\ [C_{surface}] + f_d\ [C_{douple}] + f_v\ [C_{voulume}]. \tag{2.24}$$

According to this model, the measured power P may be decomposed into three quantities:

$$P_s = f_s\ (1 + \beta\hat{}2) \qquad P_d = f_d\ (1 + \alpha\hat{}2) \qquad P_v = \frac{8}{3} f_v. \tag{2.25}$$

where the total power is calculated as:

$$P = P_s + P_d + P_v \tag{2.26}$$

2.2.2.2. Yamaguchi Decomposition

Yamaguchi came up with one more component with which the three major scattering mechanisms are decomposed. The fourth component is called a helix scattering matrix $[C]$, or coherency $[T]$ and can be shown as four scattering mechanisms [17]:

$$[C] = f_s\ [C_{surface}] + f_d\ [C_{douple}] + f_v\ [C_{voulume}] + f_c\ [C_{helix}]. \tag{2.27}$$

where f_s, f_d, f_v and f_c are the expansion coefficients. Also $[C_{voulume}]$ is calculated from the following formula:

$$10 \log\ [S_{HH}^2]\ /\ [S_{VV}^2] \tag{2.28}$$

Finally, the scattering power will be as follows:

$$P_s = f_s\ (1 + \beta\hat{}2) \qquad P_d = f_d\ (1 + \alpha\hat{}2)$$

$$P_v = f_v \qquad P_c = f_c. \tag{2.29}$$

where the total power calculated as:

$$P = P_s + P_d + P_v + P_c \tag{2.30}$$

Different theorems of polarimetric decomposition were applied to compare the results of different theorems using DLR ESAR L-band full polarized data. Results show that the two coherent theorems, which are Pauli decomposition and Cameron decomposition, work better in detecting nature targets, while SDH is suitable for man-made targets. Moreover, Freeman decomposition from incoherent decomposition is suitable for detecting nature targets while Yamaguchi decomposition works better with man-made targets. Finally, by comparing the previous coherent and incoherent decomposition, it can be shown that they have quite similar results between them [13].

In conclusion, this chapter explained the basic principles of SAR polarimetry with a mathematical representation of all the matrices and equations. The chapter is concluded with synthetic aperture radar polarimetry decomposition to extract the reliable information from the backscatter. These decomposition theorems will be used in future to analyze the Waseda project data. The following chapter is a comprehensive literature review on the calibration of SAR polarimetry. The chapter is divided into two sections. The first section will explain how to calibrate a synthetic aperture radar image. Different methods will be introduced by starting with passive reflectors and active reflectors. Also, the three steps of calibrating SAR, which start by estimating and correcting the cross talk and then calibrating co-polarized channel phase imbalance, then finally, the absolute radiometric calibration. The second section introduces the phenomena of the polarization signature which is also known as a polarization response. A polarization signature is the process of displaying the received power as a function of polarization in a graphic way. In this section, two examples of polarization signatures will be introduced with their equations for power and the matrices. The first example is the trihedral corner reflector which will be used many times in our calibration. The second example is the dihedral corner reflector which will also be used in our calibration procedure, especially in overall calibration process.

3

Polarimetric Calibration

The third chapter is a comprehensive literature review on the calibration of SAR polarimetry. The chapter is divided into two sections. The first section will introduce passive corner reflectors and focus on two passive reflectors which are the trihedral and the dihedral corner reflectors with their specifications. Also, the section will introduce active calibration to show the design, and explain how active calibration can be done, as well as its major advantages over passive reflectors. Finally, the last part in section one will be on three general calibration process for polarimetric radar image data which are: cross talk estimated and corrected, co-polarized channel phase imbalance calibration, and absolute radiometric calibration. The second section in chapter three introduces the phenomena of the polarization signature which is also known as a polarization response. A polarization signature is the process of displaying the received power as a function of polarization in a graphic way. In this section, two examples of polarization signatures will be introduced with their equations for power and the matrices. The first example is the trihedral corner reflector which will be used many times in our calibration. The second example is the dihedral corner reflector which will also be used in our calibration procedure, especially in overall calibration process.

3.1. Polarimetric calibration

Initially, it wasn't a priority to calibrate image data from the SAR, but with improved technology, calibration is now the norm, and it is associated with the radar backscatter of the scene. The need for image calibration is due to the continuous use of quantitative SAR data. Scientists need it to compare data from different sensors, build up databases of backscatter from different terrain, fully undertake research geophysical applications, and many more functions that un-calibrated SAR data cannot do [18].

In the case of airborne SAR systems, a flat earth is always assumed for the purpose of calculating the radar look angle. Figure 3.1 below shows the geometry in SAR system in the case of airborne systems, where the radar platform is assumed to be at an elevation h above the reference plane. The incidence angle is equal to the look angle for a given pixel. Also, the look angle γ, is measured through the following relation [19]:

$$\gamma = cos^{-1} (h / R). \qquad (3.1)$$

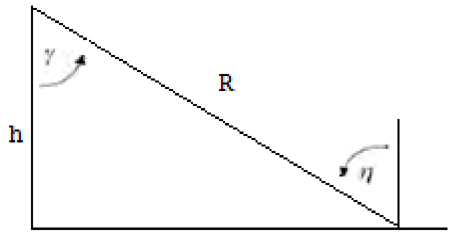

Figure 3.1: Imaging geometry for the case of an airborne SAR system [19]

Where γ represent the look angle, η represent the incidence angle, h is the altitude of the radar platform above the reference plane, and R is the slant range.

The local incidence angle changes due to terrain effects could cause effects on the radar image data. For example, radar backscattering differs with incidence angle as well as terrain slope. Once the system is calibrated, proper polarimetric feature extraction will require a digital elevation model (DEM) for the image to reduce the effect of incidence angle. It is important to note that this dissertation is not about image, pixel by pixel calibration, but about the performance of the sensor only. Also, the calibration reflectors which we will be designed for the Waseda SAR sensor will be adjusted in the field to be appropriate to the look angle for a particular flight. This means each reflector must have a means of having its elevation angle adjusted and it must be orthogonal to the flight track.

3.1.1. Passive Radar calibrators

There are many types of passive reflectors to be used as calibrating test equipment with different proprieties such as: trihedral, dihedral and spherical. A very good question to ask is; what is the optimum corner reflector for calibration of imaging radars? Kamal Sarabandi has a suitable answer. In his research on corner reflectors for calibration of imaging, he characterized the success of using external reflectors in five qualifications, which are: the radar cross section, large radar cross section pattern, physical size of the reflector, radar cross section stability, and insensitive radar cross section (RCS) to the environment around the reflectors [20].

As shown below in figure 3.2, the dihedral corner reflector has two surfaces, which are on orthogonal planes, while the trihedral corner reflector has three. Trihedral corner reflectors are the most commonly used type for calibration of SAR images, because of their large radar cross section (RCS), as well as, they are not expensive to manufacture. The construction for the trihedral is done by joining three flat triangular panels with an aluminum frame, then the panels are bolted together to create the trihedral corner reflector. To reduce the weight, it is covered by aluminum mesh. Trihedral corner reflectors generate co-polarized radar return only, and do not work as reflectors for cross polarization [19].

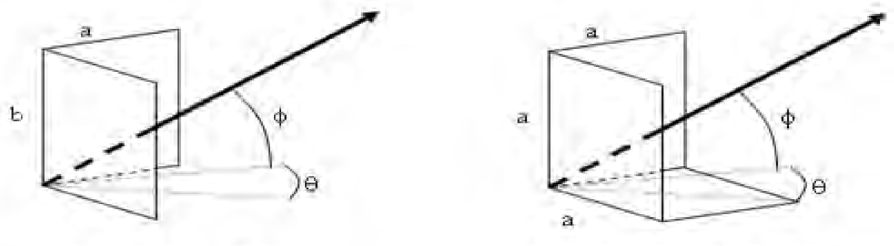

Dihedral corner reflector
A

Trihedral corner reflector
B

Figure 3.2: Dihedral and trihedral corner reflector geometry [21]

Where θ represent the angle between the radar sight line and the project line of the symmetry axis of the corner reflector on the datum plane, and ϕ represent the angle between the symmetry axis and its project line on the datum plane. The length of the leg for the corner reflector is represented by a and b. The maximum radar cross section for trihedral corner reflectors is shown below in table 3.1, where λ is the radar wavelength. The maximum radar cross section (RCS) occurs only for the co-polarized channels HH and VV, where the scattering matrix is the identity matrix.

Table 3.1: RCSs of the most common reflectors [21]

Types of canonical reflectors	Maximum RCS (m^2)
Triangular trihedral	$4\pi a^4/3\lambda^2$
Rectangular dihedral	$8\pi a^4/\lambda^2$

The dihedral corner reflector has a maximum radar cross section (RCS) shown in table 3.1 above, and the scattering matrix for the dihedral depends on the orientation angle for the dihedral, with respect to the line of sight to the radar. The orientation angle controls the polarization states, for which the maximum radar cross section (RCS) applies. If the orientation angle is equal to 0, it means that the maximum radar cross section (RCS) occurs only for the co-polarized channels HH and VV. The dihedral corner reflector has a number of disadvantages over the trihedral corner reflector. One of the disadvantages is the difficulty of deploying the dihedral on the field, because of the measurements of the orientation angle, with respect to the radar.

3.1.2 Active Radar calibrators (ARCs)

Another way of implementing the calibration for the radar image is to build an active radar calibrator instead of the passive reflector. As shown below in figure 3.3, the schematic of an active radar calibrator consists of a receiving antenna, transmitting antenna, and an amplifier between them. The idea behind the active radar is to detect the energy and then amplify it, and transmit the signal again to the radar at a known level.

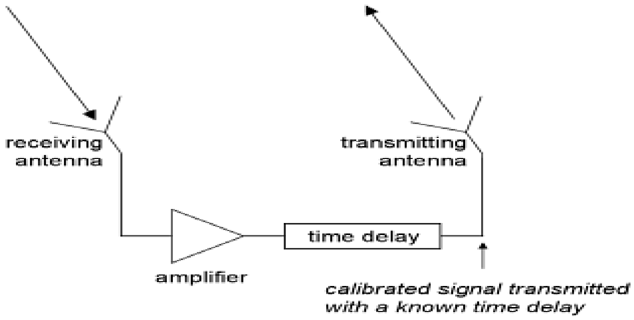

Figure 3.3: Schematic of an active radar calibrator [12]

Active radar calibrators have become a popular tool for SAR calibration in recent years. Much of research is being done using the active radar calibrator (ARC) to show the advantages of using the active radar calibrator (ARC) over passive reflectors. Brunfeldt and Ulaby presented a paper [22] on active radar calibrators, and they came up with a number of advantages, as well as limitations, of using active radar calibrator (ARC) over passive reflectors. One of the advantages is the suitability of active radar calibrator (ARC) for calibration in any polarization configurations. Also, the signal, which is transmitted by the active radar calibrator (ARC), is larger than the one which is scattered by the passive reflectors. Moreover, the active radar calibrator is smaller in size.

The limitation of active radar calibrators is the limits of the maximum amplifier gain, which can be used because of the mutual coupling between transmit and receive antennas of the active radar calibrator (ARC). Also, the need for power to operate the active radar calibrator is another disadvantage. Finally, Brunfeldt and Ulaby concluded that the active radar calibrator is a better choice to use if the calibration configuration needs a reflector, which can provide a large radar cross section as well as the calibration of cross polarized.

3.1.3. Calibration Process for Polarimetric Radar Image

The measurements of radar polarimetry have to be calibrated to get accurate data. The calibration for polarimetric radar measurements is done in steps and procedures, which will be explained in detail in this section. There are three general calibration processes for polarimetric radar image data, which are as follows:

3.1.3.1. The cross talk parameters are estimated and corrected:

The full scattering matrices for all the image pixels are measured using a radar polarimeter. It records all the data on the scattering process in the transverse components of the magnetic or electric fields. Polarimetric calibration identifies the 2×2 distortion matrix of polarimetric SAR data, by showing the polarimetric transformation between the receivers and transmitters, and it also calibrates any un-calibrated SAR data with the polarimetric distortion matrices [23].

Several polarimetric Crosstalk Calibration (PCTC) methods have been developed since the early 1990s based on distributed natural targets. The major assumption is that the like and cross-polarized of the scattering matrix are uncorrelated. [24]

In 1990, Van Zyl [25] developed a method to estimate the cross talk for scattering matrix data with assuming the reciprocal on transmit and receive for the radar system. The method is based on the theoretical result that for natural targets with azimuthal symmetry. The method was applied by Van Zyl to compressed data produced by the JPL aircraft SAR. The measured scattering matrices are symmetrized due to the model of the system as reciprocal, therefore:

$$[\mathrm{E}]=[\mathrm{E}]^{T}. \tag{3.2}$$

where [E] represents the symmetrized measured scattering matrix and the superscript T represents the transpose of the matrix. Van Zyl used the following system model showing the effects of both transmitting and receiving systems on symmetrized scattering matrix.

$$[\mathrm{E}] = \mathrm{A}e^{i\phi}\ [\mathrm{R}]\ [\mathrm{S}]\ [\mathrm{T}]. \tag{3.3}$$

where [R] represents the polarization distortion of the receive channel, [T] represents the polarization distortion of the transmit channel, [S] represents the desired scattering matrix from the target, factor A represents the overall absolute amplitude, and finally, the phase from the round trip propagation is represented by ϕ. The measured scattering matrix can be written as follow:

$$[\mathrm{E}] = \mathrm{A}e^{i\phi}\begin{bmatrix}1 & \delta_2\\ \delta_1 & f\end{bmatrix}[\mathrm{S}]\begin{bmatrix}1 & \delta_1\\ \delta_2 & f\end{bmatrix}. \qquad (3.4)$$

where δ_1 is a complex number representing the cross talk when vertically polarized transmitted or received, δ_2 represents the cross talk when horizontally polarized transmitted or received, and f represents the one-way co-polarized channel imbalance in amplitude and phase. It is important to note that the system is written as:

$$\begin{bmatrix}1 & \delta_1\\ \delta_2 & f\end{bmatrix} = \begin{bmatrix}1 & 0\\ 0 & f\end{bmatrix}\begin{bmatrix}1 & \delta_1\\ \delta_2/f & 1\end{bmatrix} \quad \text{or} \quad [\mathrm{T}] = [T_c]\,[T_x]. \qquad (3.5)$$

Also, [R] = $[R_c]$ $[R_x]$ can be written in the same manner where $[R_c]$ = $[T_c]$ and $[R_x]$ =$[T_x]^T$. Therefore, the measured scattering matrix can be written as follows:

$$[\mathrm{E}] = [R_x]\,[\mathrm{W}]\,[T_x]. \qquad (3.6)$$

where [W] is the amplitude imbalance and absolute calibration steps and represented as follows:

$$[\mathrm{W}] = \mathrm{A}e^{i\phi}\,[R_c]\,[\mathrm{S}]\,[T_c]. \qquad (3.7)$$

The parameters δ_1 and δ_2/f are in the $[R_x]$ and $[T_x]$ matrices. They are estimated from equation [E] with the knowledge of the measured element of [E] as well as known the value of $<W_{hv}W_{hv}^*>$. The measurements are based on the two assumptions which are as follows:

1- $\delta_1$and δ_2 are small compared to 1 implying the system is well isolated.

2- The components of scattering matrix for both co-and cross-components are uncorrelated. That means $<W_{hh}^*W_{hv}>$ = 0 and $<W_{vv}^*W_{hv}>$ = 0 (Which is also true with element [S].

Finally, an initial value of δ_1=δ_2/f=0 used for estimating $<W_{hv}W_{hv}^*>$ from equation below then first guess for the parameters of cross talk calculated using equation [E] and so on until reaching stable estimate. The cross talk achieved by calculating the following equation [26]:

$$[\mathrm{W}] = [R_x]^{-1}[\mathrm{E}]\,[T_x]^{-1} \qquad (3.8)$$

In 1994, a direct method by Quegan [27] designed for scattering matrix data without assuming the reciprocal on transmit and receive for the radar system. However, other assumptions were made about the radar system and the distributed targets: The reciprocal for all the scatterers, both like and cross-polarized return to be uncorrelated as well as small cross talk terms to be small. Quegan used the following model to describe the radar system:

$$\begin{bmatrix} o_{hh} & o_{hv} \\ o_{vh} & o_{vv} \end{bmatrix} = \begin{bmatrix} r_{hh} & r_{hv} \\ r_{vh} & r_{vv} \end{bmatrix} \begin{bmatrix} s_{hh} & s_{hv} \\ s_{vh} & s_{vv} \end{bmatrix} \begin{bmatrix} t_{hh} & t_{hv} \\ t_{vh} & t_{vv} \end{bmatrix}. \qquad (3.9)$$

where the o matrix represents the observed scattering matrix which measured from the radar system and s matrix represents the ideal scattering matrix from the observed target. Also, s_{hv} is the complex scattering amplitude for both h-receive and v-transmit polarization. The quantity $t_{hv}$is the transmission in channel h when channel v is excited, and r_{hv} is the response in channel h to a stimulus in channel v [28]. Converting the scattering matrix to a vector format and writing the model as follows [24]:

$$\begin{bmatrix} o_{hh} \\ o_{vh} \\ o_{hv} \\ o_{vv} \end{bmatrix} = Y \begin{bmatrix} \alpha & v+\alpha w & vw \\ \alpha u & \alpha & v \\ \alpha z & 1 & w \\ \alpha uz & u+\alpha z & 1 \end{bmatrix} \begin{bmatrix} K^2 & 0 & 0 \\ 0 & K & 0 \\ 0 & 0 & 1 \end{bmatrix} \begin{bmatrix} S_{hh} \\ S_{hv} \\ S_{vv} \end{bmatrix}. \qquad (3.10)$$

where Y is the overall system gain in the VV channel Y = $\frac{r_{vv}}{t_{vv}}$, K is the receive channel imbalance K= $\frac{r_{hh}}{r_{vv}}$, and α is the ratio of the receive and transmit channel imbalance $\alpha = (r_{vv}t_{hh})/(r_{hh}t_{vv})$. The cross talk terms can be estimated using the following relation:

$$\text{z}=\frac{t_{hv}}{t_{hh}}\ , \quad \text{v}=\frac{t_{vh}}{t_{vv}}, \quad \text{w}=\frac{r_{hv}}{r_{vv}}, \quad \text{u}=\frac{r_{vh}}{r_{hh}} \qquad (3.11)$$

In 1992, iterative method by Klein [29] using the same assumptions in Quegan method but with another definition for the scattering matrix elements where s_{hv} is the complex scattering amplitude for both h-transmit and v-receive polarization. The model is represents as follows:

$$\begin{bmatrix} O_{hh} & O_{hv} \\ O_{vh} & O_{vv} \end{bmatrix} = \begin{bmatrix} R_{hh} & R_{hv} \\ R_{vh} & R_{vv} \end{bmatrix} \begin{bmatrix} S_{hh} & S_{hv} \\ S_{vh} & S_{vv} \end{bmatrix} \begin{bmatrix} T_{hh} & T_{hv} \\ T_{hh} & T_{vv} \end{bmatrix}. \qquad (3.12)$$

where the transmission in channel v represented by the quantity $T_{hv}$when channel h is excited, and R_{hv} is the response in channel h to a stimulus in channel v. The cross talk terms can be estimated using the following relation by Klein [28]:

$$\check{T}_{hv} = \frac{T_{hv}}{T_{vv}}\ , \quad \check{T}_{vh}=\frac{T_{vh}}{t_{vv}}, \quad \acute{R}_{hv}=\frac{R_{hv}}{R_{vv}}, \quad \acute{R}_{vh}=\frac{R_{vh}}{R_{hh}} \qquad (3.13)$$

The relation between the cross talk terms for Klein and Quegan as follows:

$$\text{z}=\check{T}_{vh}\ , \quad \text{v}=\check{T}_{hv}, \quad \text{w}=\acute{R}_{hv}, \quad \text{u}=\acute{R}_{vh} \qquad (3.14)$$

In 2006, T.L. Ainsworth presented a posteriori method [30] to calibrate polarimetric SAR data. It calibrated crosstalk in the channels, and imbalance in their gains, using only the observed polarimetric SAR data without the reflection symmetry assumption. Converting the scattering matrix to a vector format and writing the model in (3.9) as follows [24]:

$$\begin{bmatrix} o_{hh} \\ o_{vh} \\ o_{hv} \\ o_{vv} \end{bmatrix} = \begin{bmatrix} k\alpha & v\alpha^{-1} & w\alpha & vwk^{-1}\alpha^{-1} \\ zk\alpha & \alpha^{-1} & wz\alpha & wk^{-1}\alpha^{-1} \\ uk\alpha & uv\alpha^{-1} & \alpha & vk^{-1}\alpha^{-1} \\ uzk\alpha & u\alpha^{-1} & z\alpha & k^{-1}\alpha^{-1} \end{bmatrix} . \begin{bmatrix} s_{hh} \\ s_{vh} \\ s_{hv} \\ s_{vv} \end{bmatrix} = [M]. \begin{bmatrix} s_{hh} \\ s_{vh} \\ s_{hv} \\ s_{vv} \end{bmatrix}. \qquad (3.15)$$

where k and α represent the channel imbalance with the following definition:

$$k = \frac{r_{hh}}{r_{vv}} \qquad \text{and} \qquad \alpha = (r_{vv}t_{hh}) / \, (r_{hh}t_{vv}). \qquad (3.16)$$

The cross talk terms can be estimated using the following relation:

$$z = \frac{t_{hv}}{t_{hh}} \;, \qquad v = \frac{t_{vh}}{t_{vv}}, \qquad w = \frac{r_{hv}}{r_{vv}}, \qquad u = \frac{r_{vh}}{r_{hh}} \,. \qquad (3.17)$$

All the previous four methods share one common assumption which is the scattering reciprocity but Van Zyl used one more which is the system symmetry. Van Zyl and Quegan methods have been more focused on estimating and removing cross talk parameters. Van Zyl method is less general than Quegan method for cross talk estimation. The model by Van Zyl was applied to NASA/JPL AIRSAR polarimetric data and show that the model is only applicable to data that have been symmetrized [19]. Klein's and Quegan's methods were applied to the Danish polarimetric airborne SAR (EMISAR) [28]. The two methods were evaluated on three data sets acquired by the MISAR. The results show that Quegan method has the most robust results and similar to results from corner reflectors. Also, Quegan's and Ainsworth's methods were evaluated for crosstalk calibration using uninhabited aerial vehicle synthetic aperture radar (UAVSAR) [31]. The results show that the method of Quegan gives crosstalk estimates that depend on target type, while Ainsworth's method gives more stable crosstalk estimates. Moreover, Ainsworth's method performs well for quad polarized data with low crosstalk, but it is no longer applicable for data with high crosstalk while Quegan's method still applicable for high crosstalk [32].

Ainsworth's method for estimating the cross talk can be easily affected by the value of k. If the value of k is more close to one, the accuracy of crosstalk is better. But if k is far to one, the accuracy of crosstalk is unstable [33].

3.1.3.2. Co-polarized channel phase imbalance calibration:

The second step in the calibration process is to calibrate the phase and amplitude for the co-polarized channels. This step can be done by using external devices, such as trihedral corner reflectors to correct any co-polarized channel imbalance. Two cases will be introduced, which are having, or not having a calibration tone built into the radar system to accomplish the co-polarized channel imbalance. In the case of a calibration tone built into the radar system, and using internal signals to do the calibration, the radar hardware has to be stable over time and the external device will be used at some point to verify the system calibration. But, if there is no calibration tone built into the system or the system is not stable, the optimum way is doing the process, dependent on external devices [19]. Van Zyl and Lou [34] introduced a system with a calibration signal, shown below in figure 3.4, to calibrate relative phases without any assumptions.

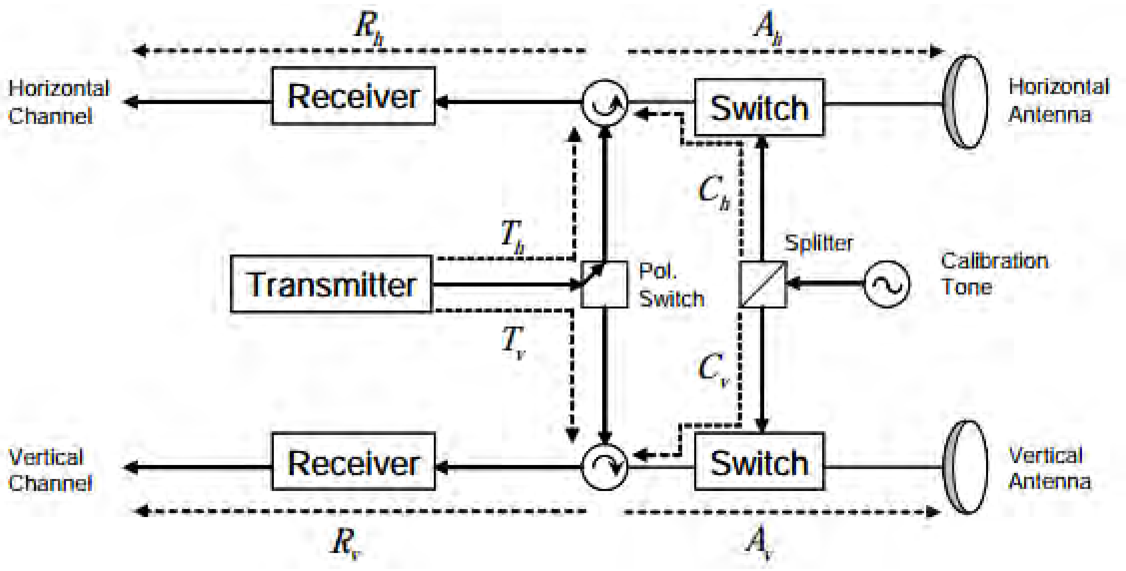

Figure 3.4: The system model for the NASA/DC-8 radar polarimeter, used by Lou and Van Zyl for co-polarized calibration [34]

The dotted lines show phase paths for the four polarization channels *(hh, hv, vh, vv).*From the scattering matrix S, and applying the previous phase differences, the measures scattering matrix R can be written as follows:

$$\mathrm{R} = \begin{bmatrix} S_{hh} \exp j\,(\text{Ø}_{t,h} + 2\text{Ø}_{a,h} + \text{Ø}_{r,h}) & S_{hv} \exp j\,(\text{Ø}_{t,v} + \text{Ø}_{a,h} + \text{Ø}_{a,v} + \text{Ø}_{r,h}) \\ S_{vh} \exp j\,(\text{Ø}_{t,h} + \text{Ø}_{a,h} + \text{Ø}_{a,v} + \text{Ø}_{r,v}) & S_{vv} \exp j\,(\text{Ø}_{t,v} + 2\text{Ø}_{a,v} + \text{Ø}_{r,v}) \end{bmatrix}. \qquad (3.18)$$

where $\text{Ø}_{t,h}$ represents the transmit phase in the h channel, $\text{Ø}_{r,h}$ represents the receive path in the h channel, and $\text{Ø}_{a,h}$ represents the antenna phase path in the h channel. Rewriting the equation as a relative phase path between the vertical and horizontal is as follows:

$$\mathrm{R} = \exp j\,(\text{Ø}_{t,v} + 2\text{Ø}_{a,v} + \text{Ø}_{r,v}) \begin{bmatrix} S_{hh} \exp j\,(\text{Ø}_{t} + 2\text{Ø}_{a,h} + \text{Ø}_{r}) & S_{hv} \exp j\,(\text{Ø}_{r} + \text{Ø}_{r}) \\ S_{vh} \exp j\,(\text{Ø}_{t} + \text{Ø}_{a}) & S_{vv} \end{bmatrix}. \qquad (3.19)$$

where $\text{Ø}_{t} = \text{Ø}_{t,h} - \text{Ø}_{t,v}$, $\text{Ø}_{r} = \text{Ø}_{r,h} - \text{Ø}_{r,v}$ and $\text{Ø}_{a} = \text{Ø}_{a,h} - \text{Ø}_{a,v}$.

By having the previous three equations, we need to find values for Ø_{t} and Ø_{r} and Ø_{a}. The antenna path difference Ø_{a} can be measured when installing the radar system in the aircraft. On the other hand, the receiver path difference is measured by using the calibration tone. As shown in figure 3.4, the receiver path difference can be written as:

$$\text{Ø}_{r} = \text{Ø}_{caltone} - \text{Ø}_{c}\,. \qquad (3.20)$$

where $\text{Ø}_{caltone}$ represents phase difference, which is obtained from information of the phase for the tone, in both horizontal and vertical channels, and $\text{Ø}_{c} = \text{Ø}_{c,h} - \text{Ø}_{c,v}$ which is represented as a phase between the calibration tone, and circulator for both channels. Finally, the last phase difference, which is Ø_{t} can be measured using the reciprocity $S_{hv} = S_{vh}$ for averaging the following complex product over the image:

$$R^{*}_{hv} R_{vh} = S^{*}_{hv} S_{vh} \exp j\,(\text{Ø}_{t} - \text{Ø}_{r}). \qquad (3.21)$$

Due to the system noise, the product $R^{*}_{hv} R_{vh}$ will differ in pixels to others. The best way to obtain a good result is to average $R^{*}_{hv} R_{vh}$ over the entire scene, where the phase Ø_{t} will be as follows:

$$\text{Ø}_{t} = \text{Ø}_{hv^{*}vh} + \text{Ø}_{caltone}. \qquad (3.22)$$

where $\text{Ø}_{hv^{*}vh}$ represents $R^{*}_{hv} R_{vh}$ in a phase term.

The other case was where there is no use of internal signals and is completely dependent on the external device, or a reflection from a rough surface to calibrate the co-polarized channels. Zebker and Lou [35] shows the ability of measuring the co-polarized phase by assuming that there is a phase difference to be known in an area in the image to measure the difference (VV-HH). Figure 3.5 is the system model for an imaging radar polarimeter, which was used by Zebker and Lou for co-polarized calibration without using an internal signal.

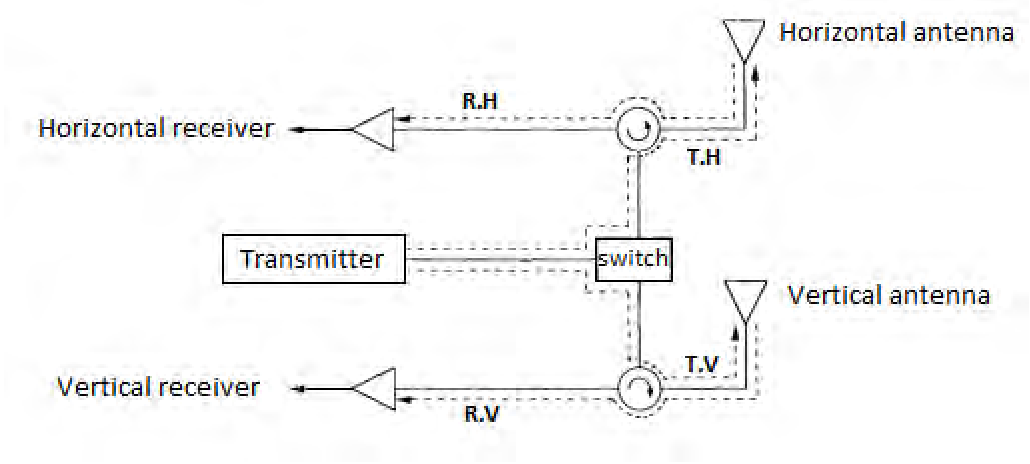

Figure 3.5: System model for an imaging radar polarimeter used by Zebker and Lou for co-polarized calibration [35]

The idea of Zebker and Lou is to have a trihedral corner reflector in the image or a reflection from a rough surface that has a co-polarized difference close to zero. After calibrating the phase, the amplitude needs to be corrected from the measured power that came from the reflector.

3.1.3.3. Absolute radiometric calibration:

The last step in the polarimetric calibration is absolute calibration. The main key in the absolute calibration is to compare the image radar cross section, which is measured to the theoretical one. Radar cross sections for each pixel can be represented as [19]:

$$\sigma_0 = K(R,\gamma) / A. \tag{3.23}$$

Where γ represents the look angle and R is the slant range. Also, A represents an area on the ground, which the scattering comes from, and calculated as follows:

$$A=\frac{\delta_r \, \delta_a}{\sin \eta} \ . \tag{3.24}$$

Where $\delta_r \, \delta_a$ represent the slant range (cross-track) and azimuth (along-track) pixel spacing, η represents the incidence angle, and K(R,γ) is determined by knowing the two parameters R and γ in figure 3.1 and calculated as:

$$\mathrm{K}(\mathrm{R},\gamma) = \frac{P_r\,(4\pi)^3 R^4}{Pt\;\lambda^2\;G_t(\gamma)\;G_r(\gamma)}\,. \tag{3.25}$$

where P_t is the transmitted power, P_r is the received power, λ is the radar wavelength, R is the distance to scattering area, $G_t(\gamma)$ is transmit antenna gain at angle γ, and $G_r(\gamma)$ is the radar look angle γ.

This technique of absolute radiometric calibration needs a good knowledge of antenna gain patterns, as well as system parameters. But according to Van Zyl [19], the best way to accomplish the absolute radiometric calibration step is by placing corner reflectors. The idea is to cover the image swath with many corner reflectors and compare the radar cross section images to theoretical values. Ruck shows the peak of the response for trihedral corner reflector as follows:

$$\sigma\,(\theta,\phi) = \frac{4\pi a^4}{\lambda^2}\left[\cos\theta\; + \sin\theta\;(\sin\phi + \cos\phi) - \frac{2}{\cos\theta + \sin\theta\;(\sin\phi + \cos\phi)}\right]^2. \tag{3.26}$$

where a represents the length of the leg for the corner reflector and λ represents the radar wavelength. The value of the angle of incidence θ is 54.74^0 and ϕ is 45^0 .The two angles θ, ϕ control the peak response for the trihedral corner reflector and have to be adjusted to obtain maximum intensity for the reflected signal.

3.2. Polarization signature

Polarization signature, which is also known as polarization response, is displaying the received power as a function of polarization in a graphic way. The scattering power can be calculated as a function of four angles, which make it difficult to represent them in a graphic way .The representation of a polarization signature for fully polarimetric data can be either co-polarized or cross polarized, where co-polarized represents the same transmitter and receiver polarization (HH and VV), while cross polarized represents the orthogonal transmitted and received polarization (HV and VH). The data is structured in the form of a scattering matrix to form the polarization signature in a 3D plot, where the x-axis shows the ellipticity between -45^0 and $+45^0$ while the y-axis shows an orientation between 0 and 180^0 [36].

In this section, two examples of a polarization signature will be introduced, with their equations for power and the matrices. The first example is a trihedral corner reflector, which will be used many times in our calibration. The second example is a dihedral corner reflector, which also will be used in our calibration procedure, especially in overall calibration processes. The scattering matrix will be introduced for each case and then present both covariance matrix and stokes matrix, as well as equations to get the polarization signature. Finally, Interactive Data Language (IDL), which is a programming language used for data analysis, will be used to write a code to show the co-polarized and cross polarized signature for each case. The results for both trihedral and dihedral corner reflectors will be a theoretical reference to compare when applying our calibration procedure in Waseda SAR sensor.

3.2.1. Trihedral Corner Reflector

The first example is the polarization signature of trihedral corner reflectors, which was introduced by Van Zyl [19] . One of the advantages for trihedral corner reflectors is the large radar cross section, which made it a suitable choice. Figure 3.3.B shows a clear idea of trihedral corner reflector geometry, which has three surfaces that are on orthogonal planes. In the trihedral reflector, the cross polarized components are zero for linear cases. The scattering matrix of a trihedral corner reflector is given by:

$$[\mathrm{S}] = C \begin{bmatrix} 1 & 0 \\ 0 & 1 \end{bmatrix}. \tag{3.27}$$

where C is calculated from the following equation:

$$\mathrm{C} = \frac{K_0\, a^2}{\sqrt{12}\pi} . \tag{3.28}$$

where a represents the length of the leg for the corner reflector and K_0 is calculated from the following equation:

$$K_0 = 2\pi/\lambda . \tag{3.29}$$

where λ represents the radar wavelength. The covariance matrix and the Stokes matrix can be calculated by using the scattering matrix, which was introduced before, with the formula of the received power in terms of scatter of covariance matrix P, as well as, the Stokes scattering operator [M].

$$\mathrm{P} = VV^* = (\hat{\mathrm{A}}\mathrm{T})(\check{\mathrm{T}}\mathrm{A})^* = \hat{\mathrm{A}}\mathrm{T}\check{\mathrm{T}}^*\mathrm{A}^* = \mathrm{A}.\,[\mathrm{C}]\,\mathrm{A}^*\,;\,[\mathrm{C}] = \mathrm{T}\check{\mathrm{T}}^* . \tag{3.30}$$

where $\hat{\mathrm{A}} = (P_h^{rec} P_h^{tr} P_h^{rec} P_v^{tr} P_v^{rec} P_h^{tr} P_v^{rec} P_v^{tr})$ is the transpose of the antenna polarization vector elements, and the scattered matrix represented by $\check{\mathrm{T}} = (S_{hh}\, S_{hv}\, S_{vh}\, S_{vv})$. The covariance matrix and Stokes matrix can be calculated as follows [19]:

$$[C]= |C|^2 \begin{bmatrix} 1 & 0 & 0 & 1 \\ 0 & 0 & 0 & 0 \\ 0 & 0 & 0 & 0 \\ 1 & 0 & 0 & 1 \end{bmatrix} \tag{3.31}$$

$$[M] = \frac{1}{2} |C|^2 \begin{bmatrix} 1 & 0 & 0 & 0 \\ 0 & 1 & 0 & 0 \\ 0 & 0 & 1 & 0 \\ 0 & 0 & 0 & -1 \end{bmatrix} \tag{3.32}$$

Finally, the received power can be found from the below calculation with two cases, which are co-polarized and cross-polarized. The positive sign is for the co-polarized, and the negative sign is for the cross-polarized response. [19]

$$P = \frac{k_0^2 a^4}{24\pi^2}\{1 \pm cos^2(2\Psi)cos^2(2\chi) \pm sin^2(2\Psi)cos^2(2\chi) \pm sin^2(2\chi)\}$$

$$= \frac{k_0^2 a^4}{24\pi^2}\{1 \pm [cos^2(2\chi) \pm sin^2(2\chi)]\}$$

$$= \frac{k_0^2 a^4}{24\pi^2}\{1 \pm cos(4\chi)\}. \tag{3.33}$$

The polarization signature of co-polarized trihedral corner reflectors is represented in Figure 3.6, using Interactive Data Language (IDL) in appendix A-1. The signature is taking positive signs from the previous power equation (3.33). X-axis shows the ellipticity between -45^0 and +45^0 while the Y-axis shows an orientation between 0 and 180^0 , where both angles relate to transmitting antenna.

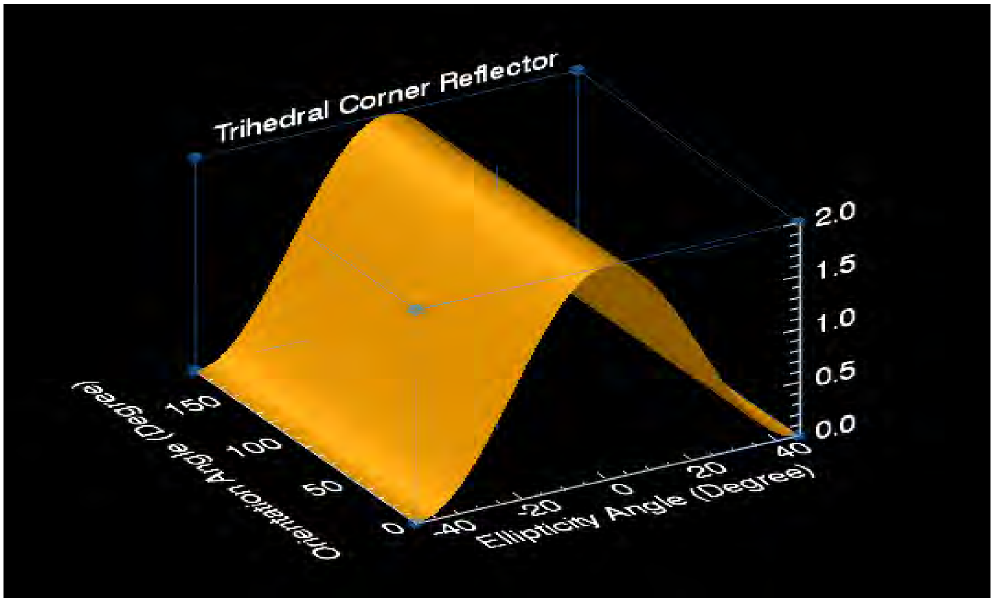

Figure 3.6: Co-polarized polarization signature for trihedral corner reflector

The maximum co-polarized response occurs if the ellipticity is zero for linear polarizations, which is a result of the derivative of the power equation with respect to ellipticity. Also, the minimum co-polarized response occurs if the ellipticity is 45^0 for circular polarization [37].

On the other hand, Figure 3.7 shows cross polarized trihedral corner reflectors taking a negative sign from the power equation (3.33), and is represented in a 3D plot using Interactive Data Language (IDL) in appendix A-2. The polarization for receiving antennae in cases of co-polarized response, is the same as transmitting one, while in cross polarized response, the polarization for receiving antennae is perpendicular to transmitting. Moreover, the case of cross polarized responses is the opposite, where maximum response occurs if the ellipticity is 45^0 for circular polarization and minimum cross response occurs if the ellipticity is zero for linear polarizations [19].

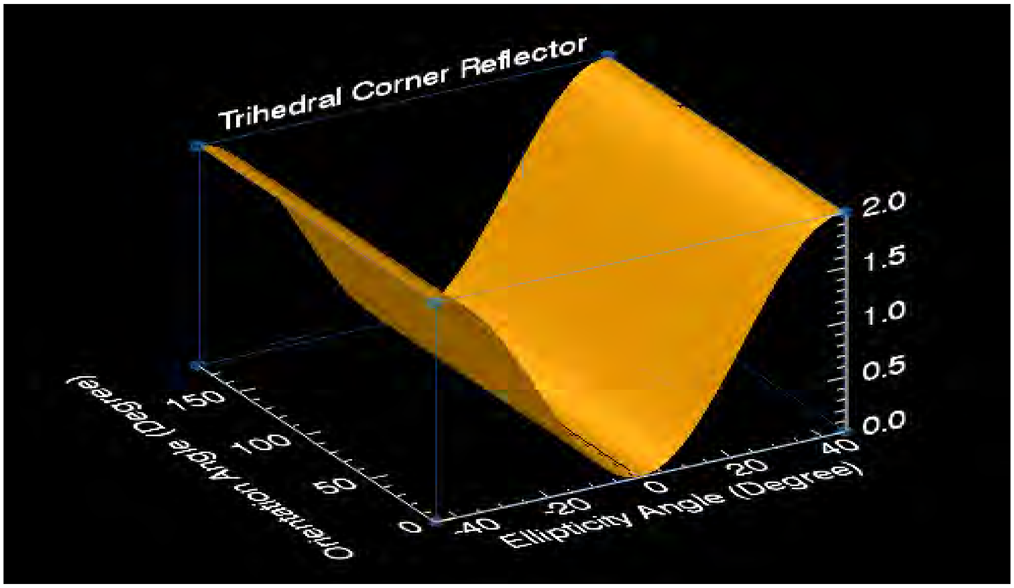

Figure 3.7: Cross polarized polarization signature for trihedral corner reflector

3.2.2. Dihedral Corner Reflector

The second example of polarization signature is a dihedral corner reflector. Figure 3.3.A gives an idea of the dihedral corner reflector geometry. There are common characteristics between trihedral and dihedral corner reflectors, such as a horizontal and vertical backscattering cross section that is identical (HH = VV), and the main difference between them is that dihedral corner reflectors are out of phase for the horizontal and vertical co-polarization components while it is in phase for the trihedral corner reflectors.

The scattering matrix, the covariance matrix, and the Stokes matrix can be calculated as follows [19]:

$$[\mathrm{S}] = C\begin{bmatrix} 1 & 0 \\ 0 & -1 \end{bmatrix}. \tag{3.34}$$

where C is calculated from the following equation:

$$\mathrm{C} = \frac{K_0\, a\, b}{\pi}. \tag{3.35}$$

where a and b represent the length of the leg for the corner reflector and K_0 is calculated from equation (3.29)

$$[\mathrm{C}] = |C|^2 \begin{bmatrix} 1 & 0 & 0 & -1 \\ 0 & 0 & 0 & 0 \\ 0 & 0 & 0 & 0 \\ -1 & 0 & 0 & 1 \end{bmatrix} \tag{3.36}$$

$$[\mathrm{M}] = \frac{1}{2}|C|^2 \begin{bmatrix} 1 & 0 & 0 & 0 \\ 0 & 1 & 0 & 0 \\ 0 & 0 & -1 & 0 \\ 0 & 0 & 0 & 1 \end{bmatrix} \tag{3.37}$$

Finally, the received power for the two cases which are co-polarized and cross-polarized, is shown as follows:

$$\begin{aligned} P &= \frac{k_0^2\, a^2 b^2}{\pi^2}\{1 \pm \cos^2(2\Psi)\cos^2(2\chi) \pm \sin^2(2\Psi)\cos^2(2\chi) \pm \sin^2(2\chi)\} \\ &= \frac{k_0^2\, a^2 b^2}{\pi^2}\{1 \pm \cos^2(2\chi)\cos(4\Psi) \pm \sin^2(2\chi)\}. \end{aligned} \tag{3.38}$$

The polarization signature of co-polarized dihedral corner reflectors is represented in Figure 3.8 using Interactive Data Language (IDL) in appendix B-1. The signature takes positive signs from power equations (3.38), and the result of the derivative shows the maximum co-polarized response which occurs at vertical and horizontal linear polarizations, as well as circular, while the minimum co-polarized response occurs at linear degree; 45^0 and 135^0 [19].

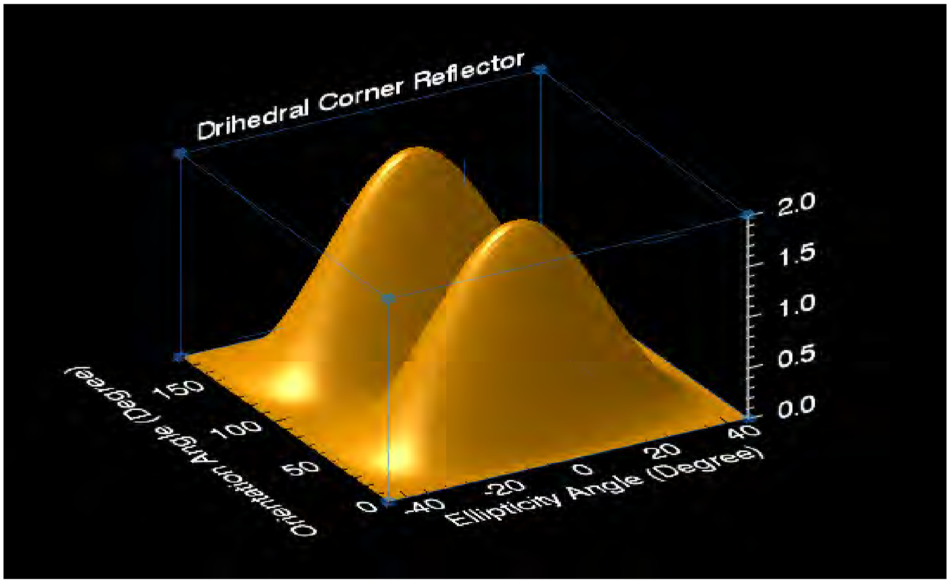

Figure 3.8: Co-polarized polarization signature for dihedral corner reflector

Another case presented in Figure 3.9, shows cross polarized signature for dihedral corner reflectors taking negative signs from the power equation (3.38), and represented in a 3D plot using Interactive Data Language (IDL) in appendix B-2 where the X-axis shows the ellipticity between -45^0 and +45^0 ,while the Y-axis shows an orientation between 0 and 180^0. Comparing cross polarized signatures with co-polarized signatures, it shows that the maximum in the case of co-polarized will be minimum in cross polarized responses, and the maximum in the case of cross polarized will be minimum in co-polarized responses.

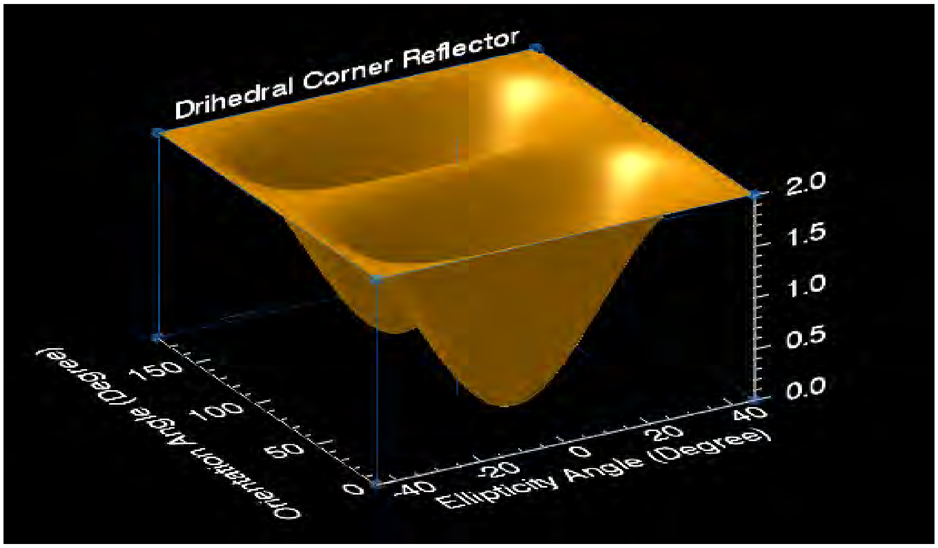

Figure 3.9: Cross polarized polarization signature for dihedral corner reflector

Finally, these techniques of calibrating SAR images are used very often in polarimetric calibration. The trihedral and dihedral corner reflectors examples are a theoretical reference to compare with our data to correct any error in the data. For example, if we deploy a trihedral corner reflector in the image, we can extract the pixel in a graphic way to show the polarization signature for the pixel that contains the trihedral corner reflector, and then compare it to the theoretical polarization signature for trihedral corner reflectors. Figure 3.10 below shows two polarization signatures for trihedral corner reflectors. The left image represents the theoretical polarization signature with no calibration error, while the right image represents a co-polarized signature with a +5 dB error.

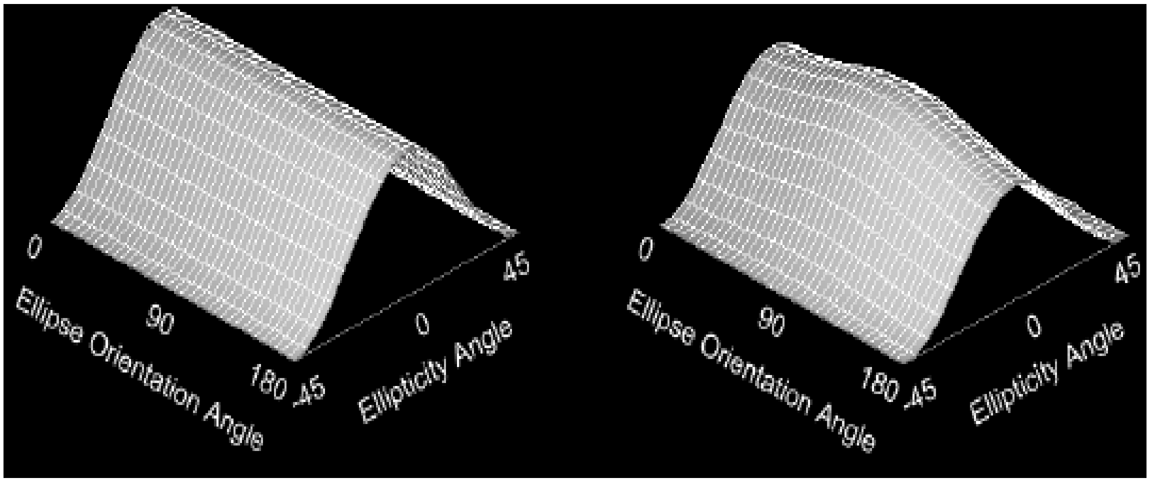

Figure 3.10: Co-polarized polarization signature for trihedral reflectors where the left image is a theoretical response and the right image with a +5 dB error [19]

In conclusion, the chapter provided excellent knowledge on different methods of SAR calibration, as well as different external devices to be used for accurate calibration results. Three general calibration process were presented for polarimetric radar image data which are: cross talk estimated and corrected, co-polarized channel phase imbalance calibration, and absolute radiometric calibration. Also, four cross talk methods were presented that share one common assumption which is the scattering reciprocity but Van Zyl used one more which is the system symmetry. Van Zyl and Quegan methods have been more focused on estimating and removing cross talk parameters. Van Zyl method is less general than Quegan method for cross talk estimation. The effect of calibration errors can be represented in a graphic way, which is called a polarization signature. The following chapter analyzes a data set, which was obtained by UAVSAR (Uninhabited Aerial Vehicle Synthetic Aperture Radar) from Jet Propulsion Laboratory (JPL). The data being analyzed is fully polarimetric calibrated data, and they will be contaminated with a high amount of coupling and the results will be discussed to show the different coupling effects on the images.

4

SAR Data Analysis

The objective of this chapter is to analyze a data which was obtained by UAVSAR (Uninhabited Aerial Vehicle Synthetic Aperture Radar) and is available for download from Jet Propulsion Laboratory (JPL). All the data sets available are calibrated SAR data. UAVSAR is a NASA L-band, fully polarimetric SAR system. The data was collected in Southern California, and is calibrated data. The objective of analyzing the data is to contaminate the calibrated data with an unrealistic high amount of coupling (-5 dB) between HH and VV, as well as between HV and both HH, VV. The reason of choosing amount of coupling (-5 dB) is because we tried other amounts such as -10 dB and it did not show a clear coupling in the images. After contaminating the data, the images will be produced to show the coupling between these channels. Finally, we picked one pixel on the image to show the difference between the pure pixel and the contaminated one, and represent them in a vector format.

4.1. UAVSAR Overview

Uninhabited Aerial Vehicle Synthetic Aperture Radar (UAVSAR) is a project which started in 2004 as an Instrument Incubator Program (IIP) by NASA. One year later, a SAR instrument was presented by JPL to NASA that met the IIP objective and it took them 4 years of design, fabrication and installation of the SAR system on a Gulfstream G-III aircraft. In 2009, UAVSAR became operational and started collecting data. UAVSAR is an L-band SAR, and has a bandwidth of 80 Mhz. Figure 4.1 below shows the Gulfstream G-III aircraft with a radar pod mounted beneath the aircraft to collect data.

Figure 4.1: Gulfstream G-III aircraft with a radar pod mounted beneath the aircraft

4.2. Data Collection

The data was collected from NASA's Uninhabited Aerial Vehicle Synthetic Aperture Radar over California; USA on 14 August 2014, and is available for the public on NASA's website for download, with a mission name Sacramento- San Joaquin Delta, CA.

The data is stored as a compressed Stokes matrix (DAT) file of multi-looked data. They have the image with three channels HH,VV and HV. Figure 4.2 below shows the collected image by UAVSAR for the mission Sacramento- San Joaquin Delta, CA. The image contains 3300 samples, as well as 14400 lines. Since the image is too large to be analyzed, a smaller region of interest was selected to be contaminated with an unrealistic high amount of coupling (-5 dB). The new region contains 459 samples and 1950 lines. The total number of samples and lines represents the number of pixels on the image. Each pixel in the image is a complex number representing a magnitude and phase, and is stored in a binary format. Every pixel in the image contains 8-bits, where the first 4-bits represent the magnitude and the last 4-bits represent the phase.

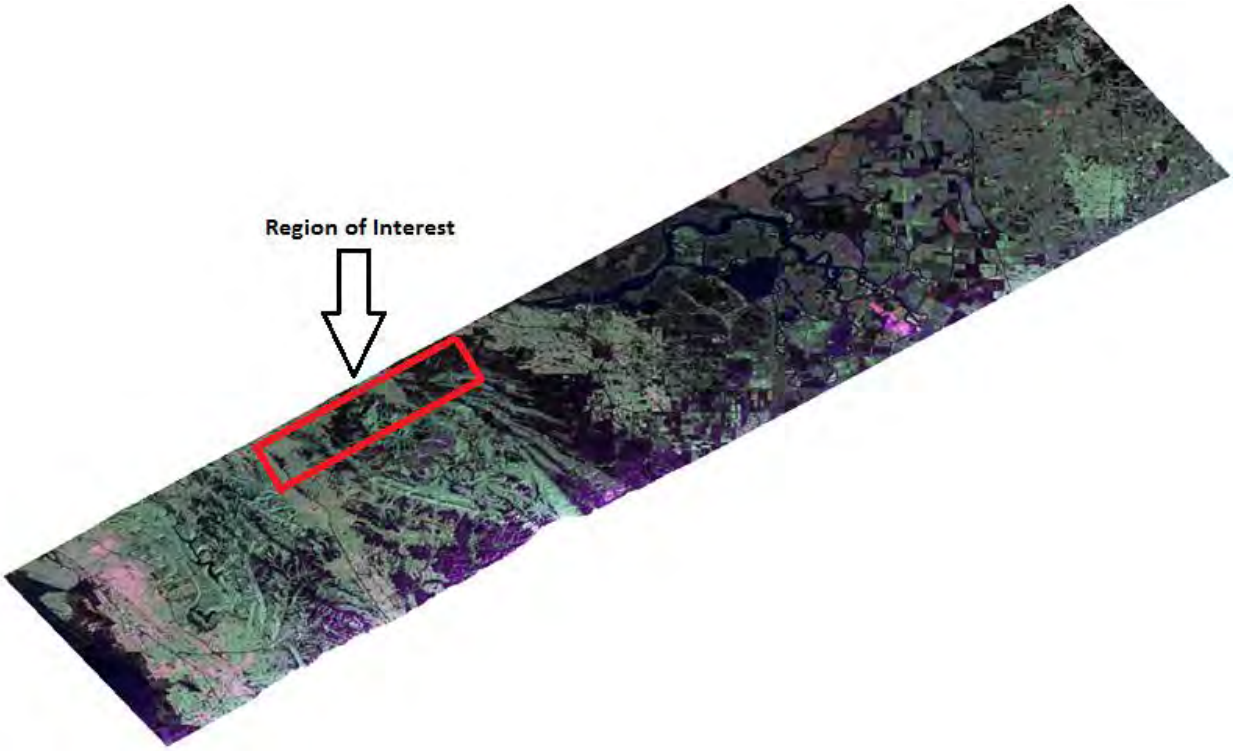

Figure 4.2 Image by UAVSAR for the mission Sacramento- San Joaquin Delta, CA contains 3300 samples, as well as 14400 lines [38]

4.3. Results and Discussion

The data is contaminated with an unrealistic amount of coupling (-5 dB) between co-polarized channels (HH and VV) by adding -5 dB from VV channel to HH channel, as well as, adding -5 dB from HH channel to VV channel. Four images will be formed for each channel to show the original image and the image after contamination, as well as the amount of contamination between the two images, and finally, a black image representing the difference between the original image and the contaminated one after removing the amount of coupling, and returning to the original.

Moreover, the HV channel will be contaminated with -5 dB by adding -5 dB from both HH and VV channels to the HV channel. Four images will be formed for the HV channel to show the original image and the image after contamination, as well as the amount of contamination between the two images, and the last image is a black image representing the difference between the original image and the contaminated one after removing the amount of coupling and returning to the original.

Finally, one pixel from each channel will be selected to represent them in a vector format. The vectors are the original pixel, the contaminated pixel with -5 dB and the difference between the original pixel and the contaminated pixel.

4.3.1. HH Contaminated Data

The data for horizontal transmitters and horizontal receivers (HH) was contaminated with an unrealistic high amount of coupling (-5 dB) from the VV channel. Each pixel in HH and VV consists of 8 bits, which represents both amplitude for the first 4 bits, and phase for the other 4 bits. The idea of contaminating the HH channel is to take -5 dB from the VV amplitude and phase, and then added to the HH channel.

Figure 4.3 below shows four images representing the coupling of -5 dB. Image 1-A shows the original image and image 1-B shows the image with -5 dB coupling. Image 1-C shows the (-5 dB) amount of contamination between the original image and the image after contamination. Finally, the last image 1-D is a black image representing the difference between the original image and the contaminated one after removing the amount of coupling and returning to the original.

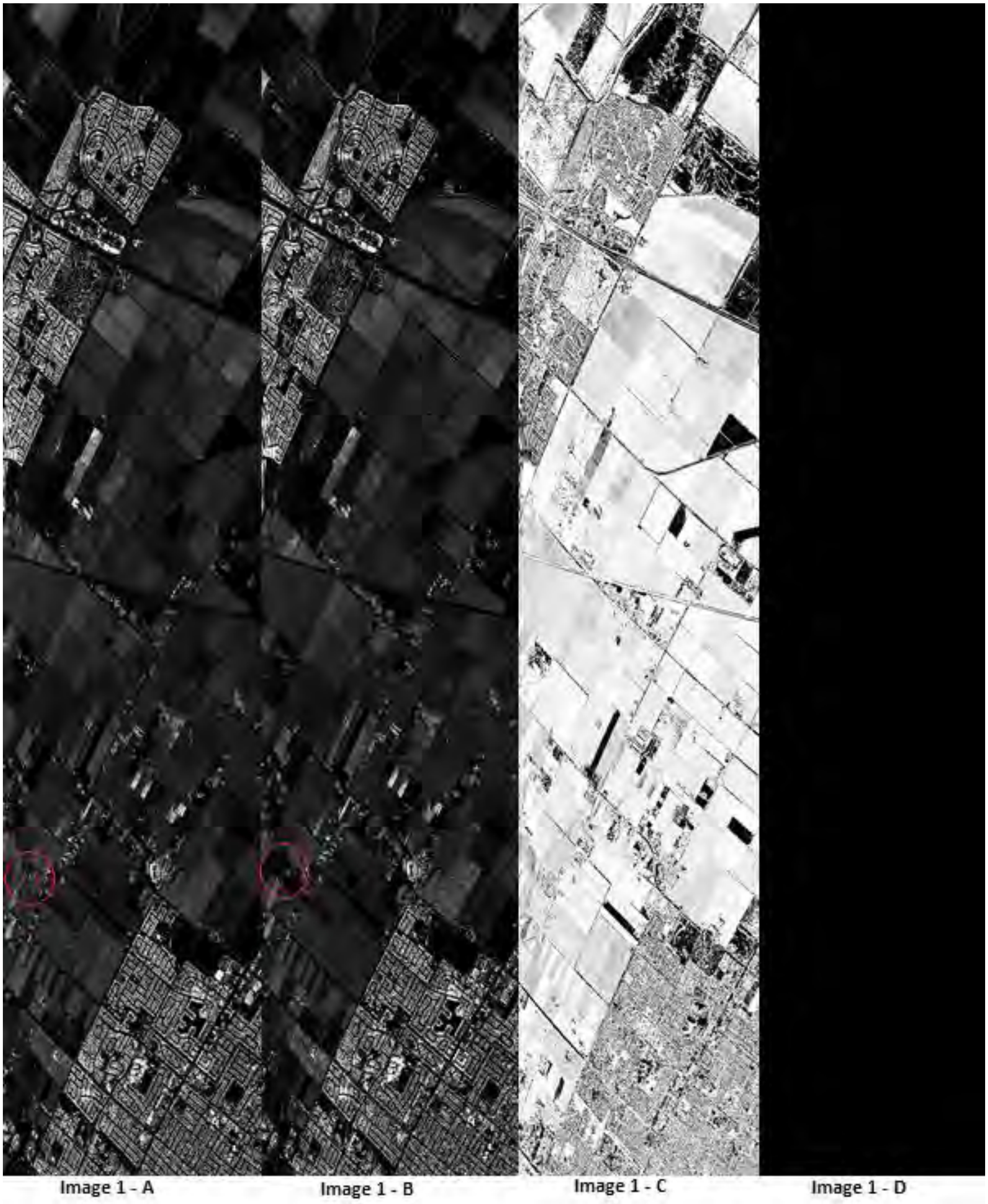

Figure 4.3: HH Contaminated data where 1-A original image, 1–B image after contamination, 1–C shows the (-5 dB) amount of contamination between the two images and 1–D is the different between the original image and the contaminated one after removing the amount of coupling and return to the original.

There is a very small amount of coupling between the original image 1-A, and the image after contamination 1-B. The red circles in the two images show the effect of the contamination on the data. As shown in the image 1-B with (-5 dB), there is some of the information is lost after contaminating the data. Figure 4.4 shows the three vectors for one pixel in the image representing the original pixel, the contaminated pixel with -5 dB and the difference between the original pixel and the contaminated pixel. Vector A represents the original image (2 + 8 j) for one pixel. To contaminate the HH data, we added (-5 dB) from VV, which has a value of (3 + 8 j). The new value which has the coupling is represented in vector B (3.69 + 12.50 j) in figure 4.4 to show (1.69 + 4.5 j) is added to vector A. Finally, vector C represents the difference between the original pixel and contaminated pixel with a value of (-1.69 - 4.5 j).

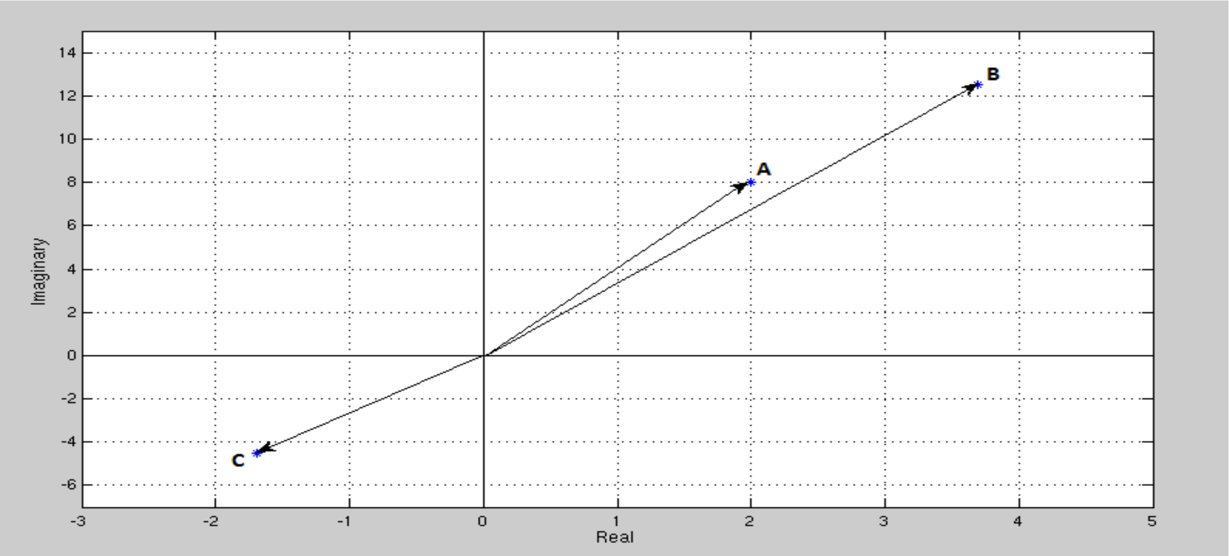

Figure 4.4: Three vectors for one HH pixel representing the original pixel, the contaminated pixel with -5 dB, and the difference between the original pixel and the contaminated pixel

4.3.2. VV Contaminated Data

The vertical transmitter and vertical receiver (VV) was contaminated with -5 dB from the HH channel. Each pixel in the HH and the VV, consists of 8 bits, which represents both amplitude for the first 4 bits and phase for the other 4 bits. The idea of contaminating the VV channel is the opposite of contaminating the HH, by taking (-5 dB) from the HH amplitude and phase, to be added to the VV channel. Figure 4.5 below shows four images representing the coupling of -5 dB. Image 2-A shows the original image and image 2-B shows the image with -5 dB coupling. Image 2-C shows the (-5 dB) amount of contamination between the original image and the image after contamination. Finally, the last image, 2-D is a black image representing the difference between the original image and the contaminated one after removing the amount of coupling and returning to the original.

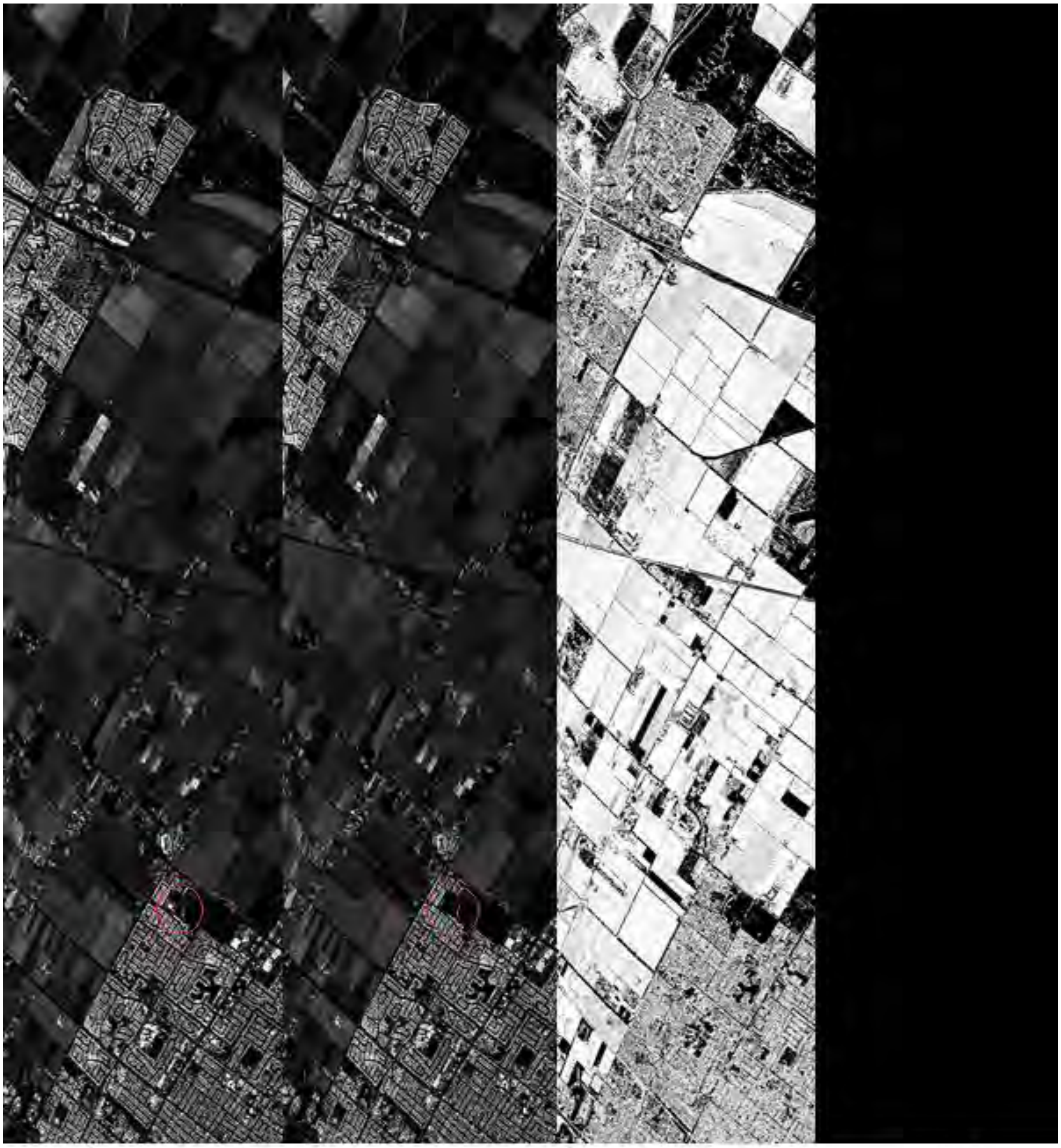

Image 2 - A
Image 2 - B
Image 2 - C
Image 2 - D

Figure 4.5: VV contaminated data where 2 - A original image, 2 – B image after contamination, 2 – C shows the (-5 dB) amount of contamination between the two images and 2 – D is the difference between the original image and the contaminated one after removing the amount of coupling and returning to the original.

There is a very small amount of coupling between the original image 2-A, and the image after contamination 2-B. The red circles in the two images show the effect of the contamination on the data. As shown above in image 2-B, there is some of the information is lost after contaminate the data with (-5 dB). Figure 4.6 shows the three vectors for one pixel in the image representing the original pixel, the contaminated pixel with -5 dB and the difference between the original pixel and the contaminated pixel. Vector D represents the original image (3 + 8 j) for one pixel. To contaminate the VV data, we added (-5 dB) from the HH, which has a value of (2 + 8 j). The new value, which has the coupling, is represented in vector E (4.125 + 12.50 j) in figure 4.6 to show (1.125 + 4.5 j) is added to vector D. Finally, vector F represents the difference between the original pixel and the contaminated pixel with a value of (-1.125 - 4.5 j).

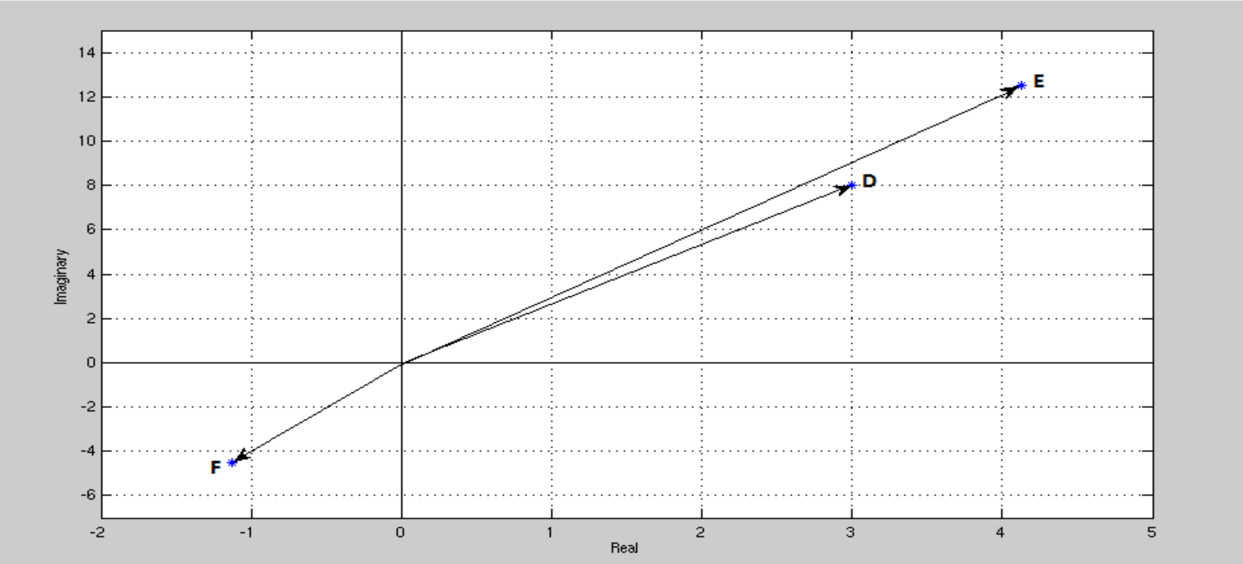

Figure 4.6: Three vectors for one VV pixel representing the original pixel, the contaminated pixel with -5 dB, and the difference between the original pixel and the contaminated pixel

4.3.3. HV Contaminated Data

The horizontal transmitter and vertical receiver (HV) was contaminated with -5 dB from both the HH and VV channels. . Figure 4.7 below shows four images representing the coupling of -5 dB. Image 3-A shows the original image, and image 3-B shows the image after contamination with amount of (-5 dB). Image 3-C shows the (-5 dB) amount of contamination between the original image and the image after contamination. Finally, the last image, 3-D, is a black image representing the difference between the original image and the contaminated one after removing the amount of coupling and returning to the original. The amount of coupling in the HV channel is more than the HH and VV because of contaminating the HV channel from the HH and VV, while the HH is contaminated from only VV as well as VV contaminated from only HH.

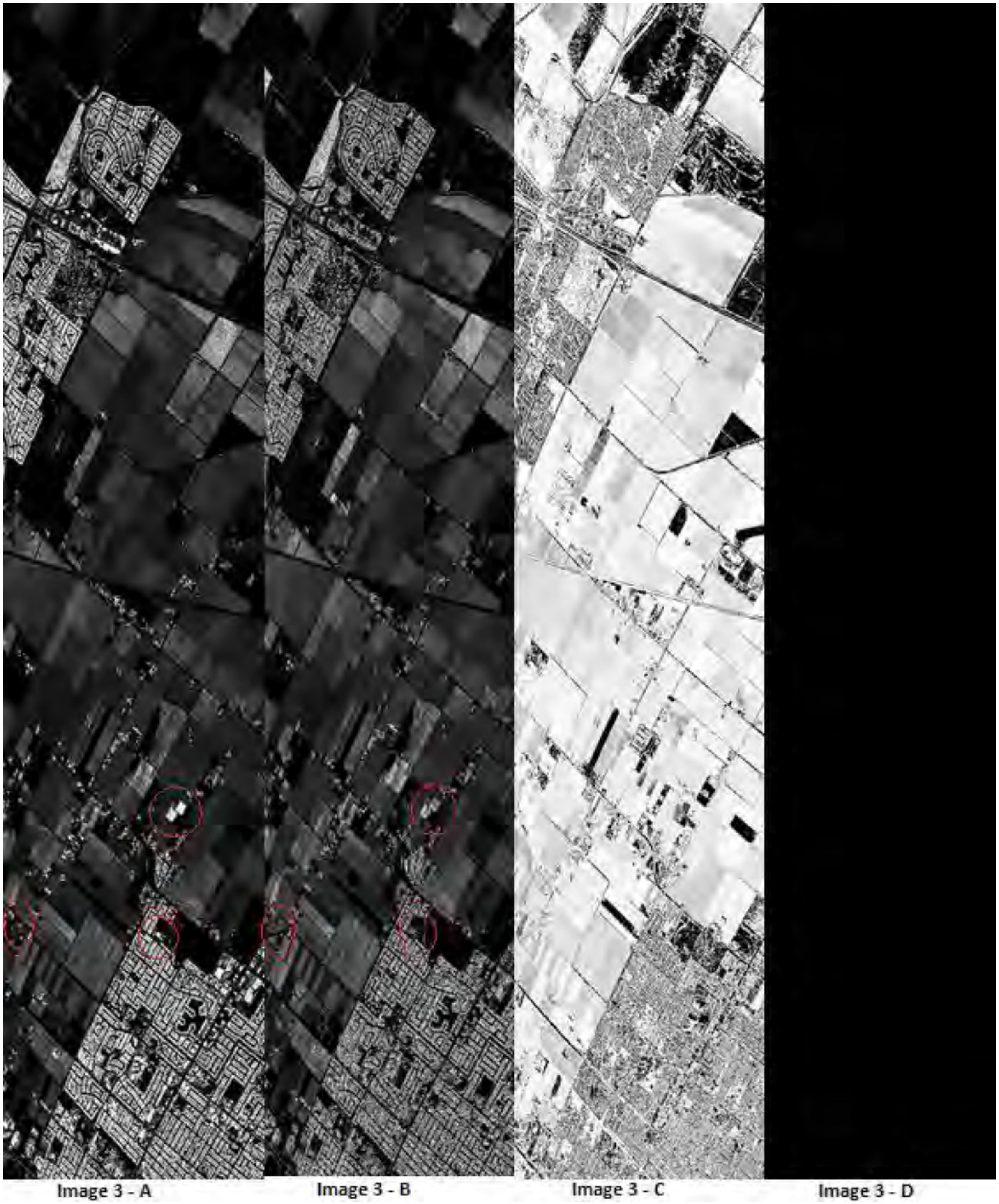

Figure 4.7: HV contaminated data where 3 - A is the original image, 3 – B is the image after contamination, 3 – C shows the amount of contamination between the two images and 3 – D is the difference between the original image and the contaminated one after removing the amount of coupling and returning to the original.

The amount of coupling in figure 4.7 between the original image 3-A, and the image after contamination with amount of (-5 dB) is higher than the HH and VV channels. The reason is because HV data was contaminated with -5 dB from both the HH and VV channels while HH and VV were contaminated with only one. Figure 4.8 shows the three vectors for one pixel in the image representing the original pixel, the contaminated pixel with -5 dB, and the difference between the original pixel and the contaminated pixel. Vector G represents the original image (1 + 6 j) for one pixel. To contaminate the HV data, we added -5 dB from both the HH and VV. The HH has a value of (2 + 8 j) and the VV has a value of (3 + 8 j). The new value, which has the coupling, is represented in vector H (3.815 + 14.998 j) in figure 4.8 to show that (2.815 + 8.998 j) is added to vector G. Finally, vector I represents the difference between the original pixel and the contaminated pixel with a value of (-2.815 - 8.998 j).

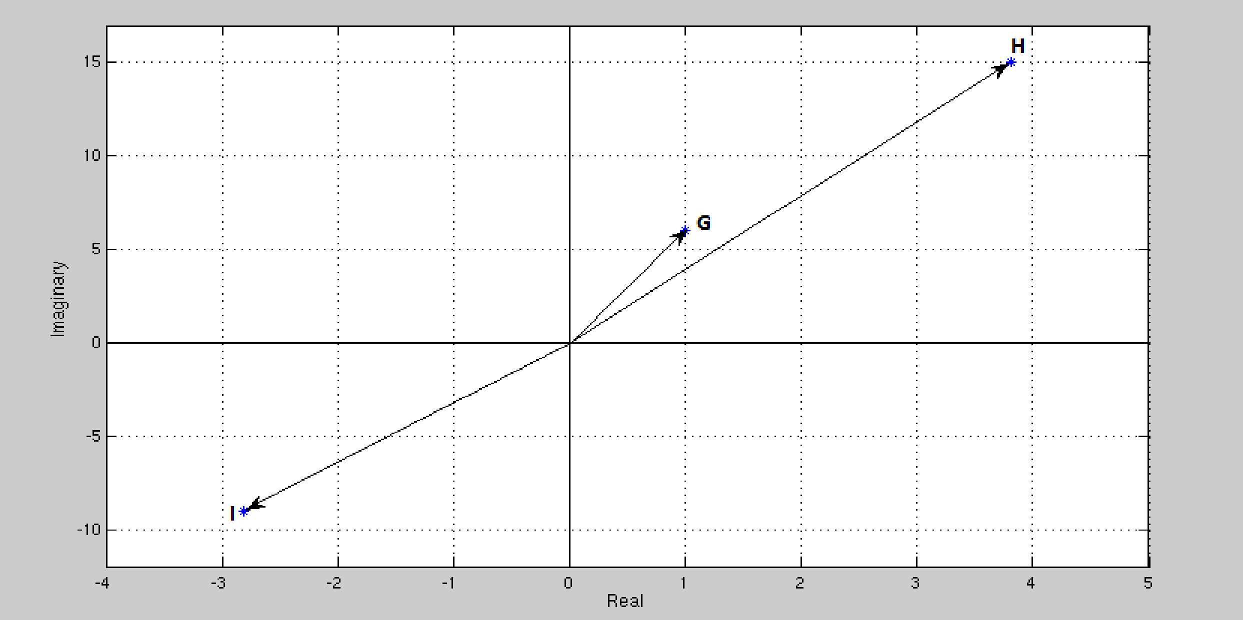

Figure 4.8: Three vectors for one HV pixel representing the original pixel, the contaminated pixel with -5 dB and the difference between the original pixel and the contaminated pixel

In conclusion, the chapter shows the effect of unrealistic amounts of coupling (-5 dB) between HH and VV as well as between the HV and both HH, VV. Also, the vector representation approved the amount of contamination for every pixel in the image. The amount of coupling for the HV channel is higher than the other two channels because -5dB from both HH and VV were added to HV. The vectors representation for one pixel proved our analysis by showing the pure value location and then the value of the vector after it is contaminated with -5 dB. The following chapter is to come up with an appreciative way of calibrating the Waseda SAR sensor from all the theories and methods that were explained in the previous chapters. The first section explains the method, and locations, of collection of data using our SAR system. The second section is a detailed polarimetric calibration procedure, which involves three steps that will be used for calibrating Waseda. The third section is on the design of the corner reflectors based on Waseda specifications. The last section is an explanation of the deployment of the corner reflectors and how the calibration flights are to be coordinated and instrumented with the reflectors.

5

Polarimetric Calibration for Waseda sensor

Chapter five summarizes all the theories and methods, which were explained in the previous chapters, and comes up with an appropriate method of calibrating Waseda. The chapter is divided into four sections. The first section explains the method, and locations, of collection of data using our SAR system. The second section is a detailed polarimetric calibration procedure, which involves three steps that will be used for calibrating Waseda. The third section is on the design of the corner reflectors based on Waseda specifications. The last section is an explanation of the deployment of the corner reflectors and how the calibration flights are to be coordinated and instrumented with the reflectors. The size for the corner reflectors to be used in Waseda was calculated for the two different bands. The size of the reflectors depend on the noise equivalent sigma zero (NESZ) curve of the radar. The fourth section in chapter five is the deployment of the corner reflectors. We will use 3000m swath width to fly with two different altitudes and place our reflectors to cover all the swath width.

Polarimetric calibration procedures will involve the following three steps in Waseda SAR project to accomplish the calibration process: the first step is to correct the cross-talk effects, using the developments by Van Zyl, by estimating the crosstalk parameters from the data itself. The second step is to correct the co-polarized channel imbalance using the Zebker and Lou assumption, which involves using trihedral corner reflectors to correct the data. The reason for using Zebker and Lou assumption is because there is no calibration tone built into the radar system in Waseda to accomplish the co-polarized channel imbalance. Also, the amplitude needs to be corrected after calibrating the phase. This step will be accomplished by measuring the power of the image using the corner reflectors.

The final step is an overall radiometric calibration using both trihedral corner reflectors and dihedral corner reflectors. According to Van Zyl [19] even if we have a good knowledge of antenna gain patterns, as well as system parameters, the best way to accomplish the absolute radiometric calibration step is by placing corner reflectors to cover the image swath. A total number of six trihedral corner reflectors and four dihedral corner reflectors will be manufactured with different sizes to be used in Waseda SAR project. The polarimetric calibration flowchart for Waseda is shown below in figure 5.1, which gives an idea of how the procedure will be implemented in Waseda SAR system.

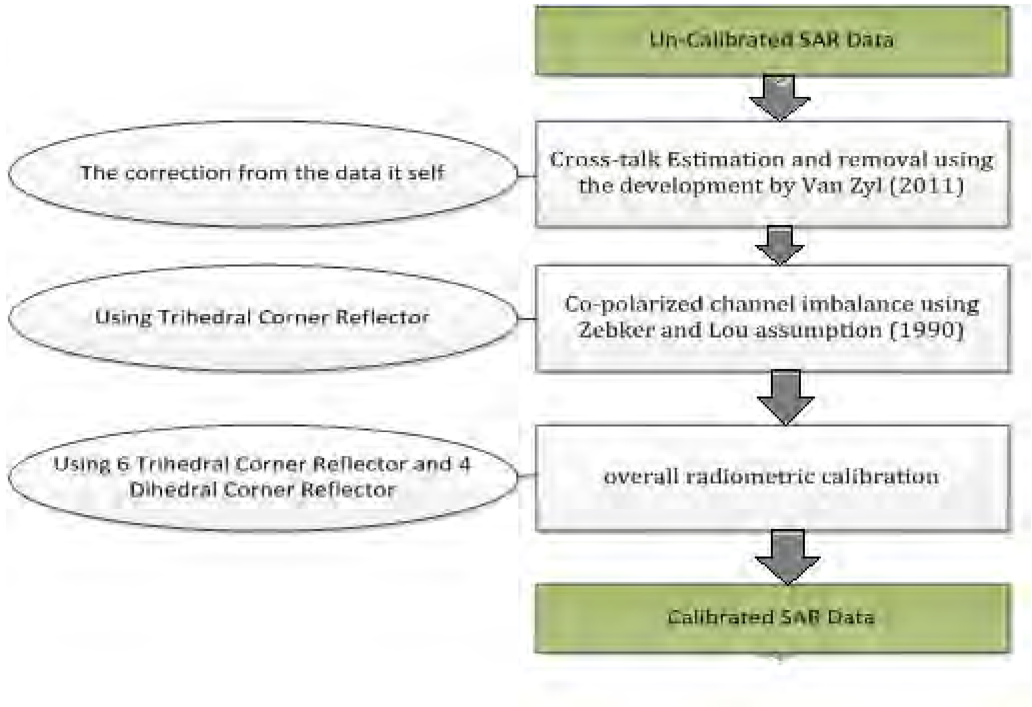

Figure 5.1: Polarimetric Calibration Flowchart for Waseda SAR System

5.1. Data collection for Waseda

The aircraft (***Cessna 208b***) or similar will be the choice for collecting the data. The data can be collected by taking off one of the doors and installing the SAR instrumentation. As shown below in figure 5.2, the aircraft can be used in Waseda. The black circle shows the door, which can be removed to install the SAR instruments, and then collect the data. Additionally, the location for collecting data will be in Riyadh, Saudi Arabia, as well as other locations to fly over, such as the Netherlands, for instruments testing. The cost and availability of aviation will play a major role in deciding on locations due to the limited budget of the project.

Figure 5.2: Aircraft which can be used in Waseda SAR project for data collection

5.2. Polarimetric calibration procedure.

The following procedure will be used for calibrating the collected images by Waseda SAR sensor .The procedure has three major steps which are: correcting and estimating the cross talk parameters, co-polarized channel phase imbalance, and absolute radiometric calibrations.

5.2.1. Cross talk parameters are estimated and corrected [19]*:*

$$\begin{bmatrix} S_{HH} & S_{HV} \\ S_{VH} & S_{VV} \end{bmatrix}_{Measured} = K\,(\gamma)\,[R_X]\ \ [R_C]\begin{bmatrix} S_{HH} & S_{HV} \\ S_{VH} & S_{VV} \end{bmatrix}_{Actual}[R_C]\ \ [T_X]. \qquad (5.1)$$

Rewriting the previous equation in vector form will be as follows:

$$\begin{bmatrix} S_{hh} \\ S_{vh} \\ S_{hv} \\ S_{vv} \end{bmatrix}_{Measured} = K\,(\gamma)\begin{bmatrix} \alpha & v+\alpha w & vw \\ \alpha u & \alpha & v \\ \alpha z & 1 & w \\ \alpha u z & u+\alpha z & 1 \end{bmatrix}\begin{bmatrix} K^2 & 0 & 0 \\ 0 & K & 0 \\ 0 & 0 & 1 \end{bmatrix}\begin{bmatrix} S_{HH} \\ S_{HV} \\ S_{VV} \end{bmatrix}_{Actual}. \qquad (5.2)$$

Then it can be represented as:

$$\begin{bmatrix} S_{hh} \\ S_{vh} \\ S_{hv} \\ S_{vv} \end{bmatrix}_{Measured} = K(\gamma)\ \ [X]\ \ \ [Q]\ \ \begin{bmatrix} S_{HH} \\ S_{HV} \\ S_{VV} \end{bmatrix}_{Actual}. \qquad (5.3)$$

The covariance matrix obtained from the previous measure vector:

$$[C]_{Measured} = |K(\gamma)|^2\ \ [X]\ \ [Q]\ \ [C]_{Actual}[X^+][Q^+]. \qquad (5.4)$$

Discovery of estimate [X] by using the assumption of reflection symmetry will have the following form:

$$[C]_{Actual} = \begin{bmatrix} < S_{HH}\,S_{HH}{}^* > & 0 & < S_{HH}\,S_{VV}{}^* > \\ 0 & S_{HV}\,S_{HV}{}^* & 0 \\ < S_{HH}\,S_{VV}{}^* > & 0 & < S_{VV}\,S_{VV}{}^* > \end{bmatrix}. \qquad (5.5)$$

And then the value of *[O]* will be formed by using multiplication from Eq. (6.2) as follows:

$$[O]=[Q][C]_{Actual}[Q^+]= \begin{bmatrix} |K^2|^2 < S_{HH}\,S_{HH}{}^* > & 0 & K^2 < S_{HH}\,S_{VV}{}^* > \\ 0 & |K^2| < S_{HV}\,S_{HV}{}^* > & 0 \\ K^{2^*} < S_{HH}\,S_{VV}{}^* > & 0 & < S_{VV}\,S_{VV}{}^* > \end{bmatrix}. \qquad (5.6)$$

Estimate the cross-talk parameters by multiplication:

$$[T] = [X]\ [O]\ [X^{+}]. \tag{5.7}$$

The following step takes out the second order terms as follows:

$$\begin{aligned}
T_{11} &\approx |\alpha|^2 O_{11} \\
T_{21} &\approx |\alpha|^2 u O_{11} + \alpha^*\ v O_{13}^* + \alpha\ (v^* + \alpha^* w^*)\, O_{22} \\
T_{31} &\approx |\alpha|^2 z O_{11} + \alpha^*\ w O_{13}^* + \alpha\ (v^* + \alpha^* w^*)\, O_{22} \\
T_{41} &\approx \alpha^* O_{13} \\
T_{22} &\approx |\alpha|^2 |u|^2 O_{11} + \alpha^* u^*\ v O_{13}^* + \alpha\, u\, v^* O_{13} + |\alpha|^2 O_{22} + |v|^2 O_{33} \\
T_{32} &\approx |\alpha|^2 u^* z O_{11} + \alpha^* u^*\ w O_{13}^* + \alpha\, z\, v^* O_{13} + \alpha O_{22} + w\, v^* O_{33} \\
T_{42} &\approx \alpha^* u^* O_{13} + v^* O_{33}^* + \alpha^*\ (u + \alpha z)\, O_{22} \\
T_{33} &\approx |\alpha|^2 |z|^2 O_{11} + \alpha^* z^*\ w O_{13}^* + \alpha\, z\, w^* O_{13} + O_{22} + |w|^2 O_{33} \\
T_{43} &\approx \alpha^* z^* O_{13}^* + w^* O_{33}^* + (u + \alpha z)\, O_{22} \\
T_{44} &\approx O_{33}.
\end{aligned} \tag{5.8}$$

Forming the following four expressions from the previous equations:

$$\begin{aligned}
T_{21} &\approx u T_{11} + v T_{41} + \alpha\ (v^* + \alpha^* w^*)\, O_{22} \\
T_{31} &\approx z T_{11} + w T_{41} + (v^* + \alpha^* w^*)\, O_{22} \\
T_{24} &\approx u T_{14} + v O_{33} + \alpha\ (u^* + \alpha^* z^*)\, O_{22} \\
T_{34} &\approx z T_{14} + w O_{33} + \alpha\ (u^* + \alpha^* z^*)\, O_{22}.
\end{aligned} \tag{5.9}$$

[T] is a Hermitian matrix to solve for u, v, z and w from the previous equations:

$$\begin{bmatrix} T_{21} - \alpha T_{31} \\ T_{24} - \alpha T_{34} \end{bmatrix} = \begin{bmatrix} T_{11} - \alpha T_{41} \\ T_{14} - \alpha T_{44} \end{bmatrix} \begin{bmatrix} u - \alpha z \\ v - \alpha w \end{bmatrix}. \tag{5.10}$$

Solution for the four parameters u, v, w and z:

$$\begin{aligned}
u &= (T_{44}T_{21} - T_{41}T_{24})/(T_{11}T_{44} - T_{14}T_{41}) \\
v &= (T_{11}T_{24} - T_{21}T_{14})/(T_{11}T_{44} - T_{14}T_{41}) \\
w &= (T_{44}T_{31} - T_{41}T_{34})/(T_{11}T_{44} - T_{14}T_{41}) \\
z &= (T_{11}T_{34} - T_{31}T_{14})/(T_{11}T_{44} - T_{14}T_{41}).
\end{aligned} \tag{5.11}$$

Solve for α from T_{32} and T_{33}:

$$\alpha = \frac{T_{32} - u^*(z\,T_{11} + w\,T_{41}) - v^*(z\,T_{41} + w\,T_{44})}{T_{33} - z^*(z\,T_{11} + w\,T_{41}) - w^*(z\,T_{41} + w\,T_{44})}. \tag{5.12}$$

Estimate of $[\dot{O}]$ after solving for [T] in (6.7):

$$[\dot{O}] = [X^+ X]^{-1} \; [X^+] \; [T] \; [X] \; [X^+ X]^{-1}. \tag{5.13}$$

Finally, initial scattering matrix data, the equivalent solution will be as follows, but it needs to recover the scattering matrix after estimating the channel imbalance:

$$\begin{bmatrix} \mathrm{K}^2 \mathrm{S}_{\mathrm{HH}} \\ \mathrm{K} \;\; \mathrm{S}_{\mathrm{HV}} \\ \mathrm{S}_{\mathrm{VV}} \end{bmatrix}_{\mathrm{Actual}} = [\mathrm{X}^+ \mathrm{X}]^{-1} \;\; [\mathrm{X}^+] \begin{bmatrix} \mathrm{S}_{\mathrm{hh}} \\ \mathrm{S}_{\mathrm{vh}} \\ \mathrm{S}_{\mathrm{hv}} \\ \mathrm{S}_{\mathrm{vv}} \end{bmatrix}_{\mathrm{Measured}} . \tag{5.14}$$

5.2.2. Co-polarized channel phase imbalance calibration

The assumption which was made by Zebker and Lou [35], to calibrate the co-polarized phase, will be used in the calibration for Waseda. The assumption is that by knowing the co-polarized phase difference (VV-HH) in an area in the image, it is possible to calibrate the co-polarized phase. The optimum device to use for measuring the co-polarized phase difference is trihedral corner reflector. Also, another solution is that the scattering from a rough surface can provide a co-polarized phase close to zero instead of using the trihedral corner reflector. The scattering matrix for a known area in the image is given by:

$$\mathrm{S} = \begin{bmatrix} S_{HH} & S_{HV} \\ S_{VH} & S_{VV} \end{bmatrix} \tag{5.15}$$

Then R matrix is what we will actually measure, instead of a received matrix ***R:***

$$\mathrm{R} = \begin{bmatrix} S_{HH} \exp j\,(\emptyset_{t,h} + \emptyset_{r,h}) & S_{HV} \exp j\,(\emptyset_{t,v} + \emptyset_{r,h}) \\ S_{VH} \exp j\,(\emptyset_{t,h} + \emptyset_{r,v}) & S_{VV} \exp j\,(\emptyset_{t,v} + \emptyset_{r,v}) \end{bmatrix}. \tag{5.16}$$

By factoring out the phase in VV:

$$\mathrm{R} = \exp j\,(\emptyset_{t,v} + \emptyset_{r,v}) \begin{bmatrix} S_{HH} \exp j\,(\emptyset_t + \emptyset_r) & S_{HV} \exp j\;\emptyset_r \\ S_{VH} \exp j\;\emptyset_t & S_{VV} \end{bmatrix}. \tag{5.17}$$

where $\emptyset_t = \emptyset_{t,h} + \emptyset_{t,v}$ and $\emptyset_r = \emptyset_{r,h} + \emptyset_{r,v}$

By having the previous two equations, we need to solve for$\O_t$ and$\O_r$.Also, using the reciprocity $S_{HV} = S_{VH}$, we will be able to find the difference $(\O_t + \O_r)$ by averaging the following complex product over the image:

$$R^*_{hv}R_{vh} = S^*_{hv}S_{vh} \exp j \,(\O_t - \O_r). \quad (5.18)$$

Knowing the co-polarized phase difference (VV-HH) in an area in the image, the two relations $\O_t + \O_r$ *and* $\O_t - \O_r$ can be found for the individual phase $\O_t$ and $\O_r$, which relates matrix R to the following matrix S:

$$\mathrm{S} = \begin{bmatrix} R_{hh} \exp - j\,(\O_t + \O_r) & R_{hv} \exp - j\,\O_r \\ R_{vh} \exp - j\,\O_t & R_{vv} \end{bmatrix}. \quad (5.19)$$

Finally, the amplitude needs to be corrected after calibrating the phase. This step will be accomplished by measuring the power of the image, which came from the trihedral corner reflector, to correct co-polarized amplitude imbalance. After estimating the cross talk parameters, removing the coupling, and correcting the co-polarized phase, we need to do the overall radiometric calibration which is the last step in our polarimetric calibration procedure, and will be explained in the next section.

5.2.3. Absolute radiometric calibration

Absolute radiometric calibrations will be done by measuring the radar cross section for a trihedral corner reflector and a dihedral corner reflector, and then comparing that to the theoretical values. Two dihedral corner reflectors will be used for each band to measure radar cross section, and compare that to the theory. Also, three trihedral corner reflectors for each band will be used, and two dihedral corner reflectors. Radar cross section for trihedral corner reflectors can be obtained from equation (3.12).

As shown in figure 3.2.B, the value of angle of incidence θ is 54.74^0 and ϕ equal to 45^0. The trihedral corner reflector will be supported by wood under the front edge. The front edge has to be parallel to the flight line. The reason for using wood is to not have a strong backscattering, and control the angles of the trihedral corner reflectors. The incidence angle for the reflector can be adjusted by raising the front edge. For example, if the incidence angle is 45^0 which is less than 54.74^0 , then we need to raise the bottom panel by a value that is equal to (54.74^0 - 45^0), which is 9.74^0. Finally, we will do a comparison of radar cross section values with theories for all the trihedral corner reflectors.

5.3. Corner reflectors design

A total number of six trihedral corner reflectors and four dihedral corner reflectors will be manufactured with different sizes to be used in Waseda SAR project. The size of the reflectors will depend on the noise equivalent sigma zero (NESZ) curve of the radar for the two bands.

5.3.1. Corner reflectors design for X-band

Three trihedral and two dihedral corner reflectors will be designed for X-band and the size of the reflectors will depend on the noise equivalent sigma zero (NESZ) curve of the radar in figure 5.3 below. A ground range of interest is selected in figure 5.3 between 2500m which represents the near range and 5500m which represents the far range. Three trihedral corner reflectors for X-band will be placed in the near range, the mid-range and the far range. Also, the other two dihedral corner reflectors for X-band will be placed only in the near range and far range.

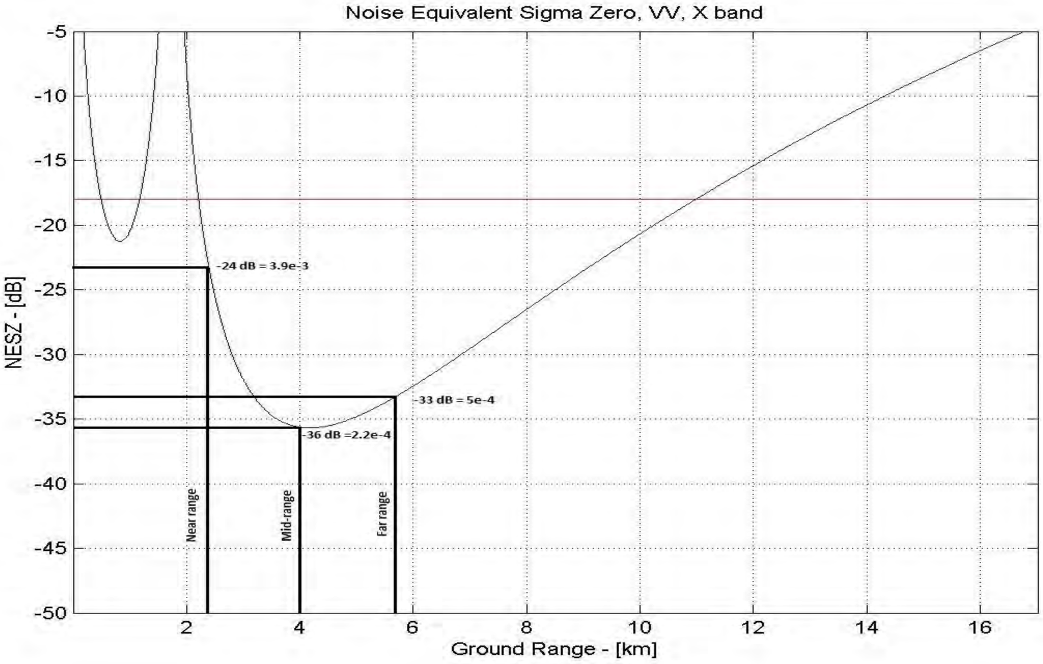

Figure 5.3: NESZ plots for X band, at VV when flying at 3000 m altitude with a look angle of 60 degrees [39]

From the System specification for the Waseda SAR sensor in table (1.1), the frequency for X-band is 9.6GHz and the wavelength is calculated as follows:

$$\lambda = C / F = (3 \times 10^8) / 9.6 \text{ GHz} = 0.03 \text{ m} \tag{5.20}$$

From table 3.1, the equation for maximum radar cross section for trihedral corner reflector is used for calculating the length of the leg for trihedral corner reflector. We want to set up the radar cross section equation for 'a' that will give radar cross section (RCS) that is 20dB greater than the noise radar cross section (RCS) at the selected ground range in figure 5.3. The equation for finding the length of the leg for trihedral reflector will be as follows:

$$100\,x = \frac{4\,\pi\,a^4}{3\,\lambda^2}\,. \tag{5.21}$$

Where ‘a’ is the length of the leg for dihedral corner reflector, λ is the wavelength for X-band, and x is value of the noise equivalent sigma zero (NESZ) multiplied by the size of the resolution cell. From the noise equivalent sigma zero (NESZ) curve in figure 5.3, we are going to find the value of x for the near range, mid-range, and far rang. The selected swath width is 3000m where near range is 2500m and the far range is 5500m. The noise equivalent sigma zero (NESZ) is -24 dB for the near range, -36 dB for the mid-range, and -33 dB for the far range. The dB value for the noise equivalent sigma zero (NESZ) is to be converted to square meters and then the value of ‘x’ is obtained by multiplying the size of the resolution cell 1X1 meter by the noise equivalent sigma zero (NESZ) then we will have the radar cross section (RCS) of the clutter target. Finally, after having the value of ‘x’, the length of the leg for trihedral corner reflector is calculated using the following equation and presented in table 5.1:

$$a^4 = \frac{3\,\lambda^2 \times 100 \times x}{4\,\pi}\,. \tag{5.22}$$

The two dihedral corner reflectors for X-band are placed only in the near and far range. From table 3.1, the equation for maximum radar cross section for dihedral corner reflector is used for calculating the length of the leg for dihedral corner reflector. Since the dihedral corner reflectors are placed in the near and far range, they will have the same value of x for trihedral corner reflector in the near and far range. The length of the leg for dihedral corner reflector is calculated using the following equation and presented in table 5.1:

$$a^4 = \frac{\lambda^2 \times 100x}{8\pi}\,. \tag{5. 23}$$

5.3.2. Corner reflectors design for P-band

Three trihedral and two dihedral corner reflectors will be designed for P-band and the size of the reflectors will depend on the noise equivalent sigma zero (NESZ) curve of the radar in figure 5.4 below. A ground range of interest is selected in figure 5.4 between 2500m which represents the near range and 5500m which represents the far range. Three trihedral corner reflectors for P-band will be placed in the near range, the mid-range and the far range. Also, the other two dihedral corner reflectors for P-band will be placed only in the near range and far range.

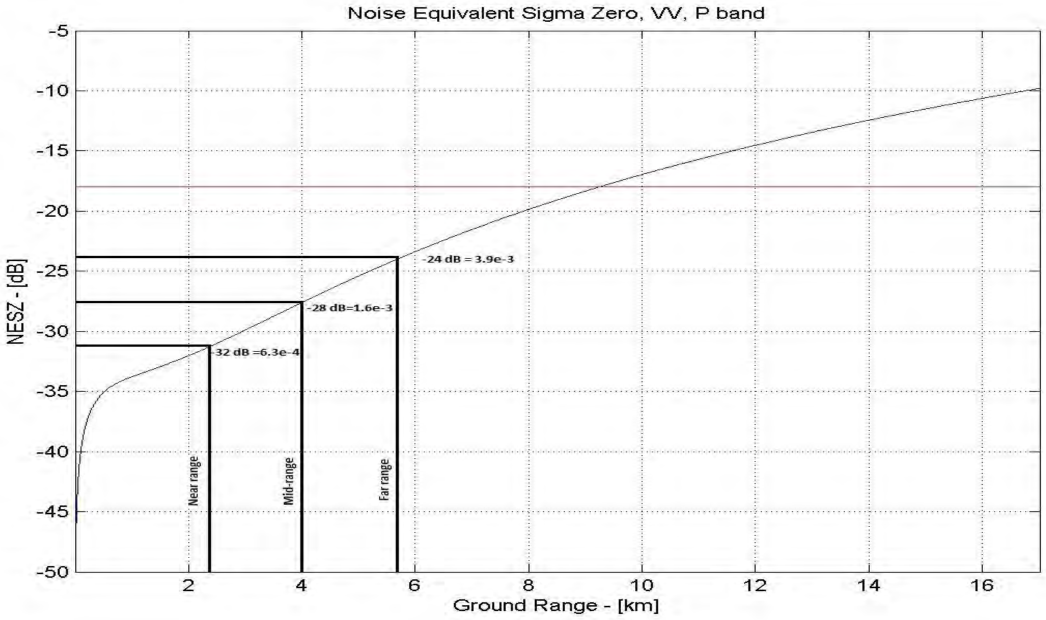

Figure 5.4: NESZ plots for P band, at VV when flying at 3000 m altitude with a look angle of 60 degrees

From the System specification for Waseda SAR sensor in table (1.1), the frequency for P-band is 500 MHz and the wavelength is calculated using equation (5.20). Also, the equation for maximum radar cross section for trihedral corner reflector in table (3.1) is used to calculate the length of the leg for trihedral corner reflector. The radar cross section equation (5.21) is used to find the length of the leg for dihedral corner reflector that will give RCS that is 20dB greater than the noise radar cross section (RCS) at the selected ground range in figure 5.4. The selected swath width is 3000 m where near range is 2500m and the far range is 5500m. The NESZ is -32 dB for the near range, -28 dB for the mid-range, and -24 dB for the far range. The value of ‘x’ is obtained by multiplying the size of the resolution cell 1X1 meter by the noise equivalent sigma zero (NESZ) then we will have the radar cross section (RCS) of the clutter target. Finally, after having the value of 'x', the length of the leg for trihedral corner reflector is calculated using equation (5.22) and presented in table 5.1.

The two dihedral corner reflectors for P-band are placed only in the near and far range. From table 3.1, the equation for maximum radar cross section for dihedral corner reflector is used for calculating the length of the leg for dihedral corner reflector. Since the dihedral corner reflectors are placed in the near and far range, they will have the same value of x for trihedral corner reflector in the near and far range. The length of the leg for dihedral corner reflector is calculated using equation (5.23) and presented in table 5.1.

Table 5.1: Results for the sizes of the reflectors in WASEDA SAR project

Ground range	**Corner reflectors sizes**			
	Trihedral corner reflector		**Dihedral corner reflector**	
	X-band	**P-band**	**X-band**	**P-band**
2500 m (near range)	0.09 m	0.27 m	0.06 m	0.17 m
4000 m (mid-range)	0.05 m	0.34 m	No dihedral reflectors in mid-range	
5500 m (far range)	0.06 m	0.43 m	0.04 m	0.27 m

Corner reflectors will be made of aluminum. The reason that aluminum was chosen is because of it is density, which results in decreasing weight. For example, comparing two trihedral corner reflectors for the same size, which are 50 cm× 50 cm × 75 cm and 2mm width, but one of them is made of aluminum and the other one is made of steel. We found that the aluminum trihedral corner reflector has a weight of 5.6 kg, while the steel trihedral corner reflector has an increased weight of 16 kg, because the aluminum density is in the range of 2.6 g/cm^3 to 2.9 g/cm^3. If we compare to steel, the density is in the range of 7.75 to 8.05 g/cm^3. [21]. Another important concern with corner reflectors is the radar cross section (RCS) sensitivity of the corner reflector. The corner angle can cause a reduction in the value of RCS due to any manufacturing error of the angle. [20]

5.4. Corner reflectors Deployment

The aircraft (*Cessna 208b*) will collect the data with two different altitudes. The first altitude is 300m and the second is 1000m. Figure 5.5 below is side-looking viewing geometry of imaging radar system. The figure gives an idea of the radar geometry and how the incidence angle is related to others where θ_f is the far range incidence angle.

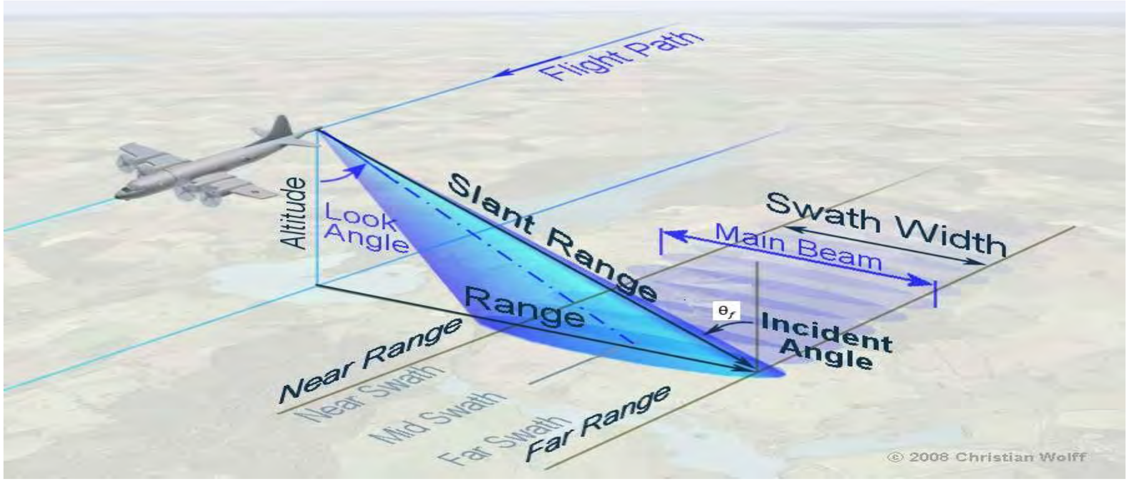

Figure 5.5: Radar Geometry [40]

The pilot will fly through points in the flight path. Figure 5.6 below shows the points from the start to the end of the flight on the flight path. The critical points are just a few hundred meters either side of the lines of calibrators. The way points are much further back and forward of the critical points. The pilot lines up on the first waypoint, and might not quite get it right. However, we will fly 2000m further on to the part where reflectors are to be imaged will be almost right and smooth, so that the autopilot should get the aircraft critically on track during the imaging, and to hit the exit point correctly. Then he has another 2000m to fly straight and turn around for the next flight. The critical points for the second flight with 1000m altitude are different because the ground track is different, due to the increased height.

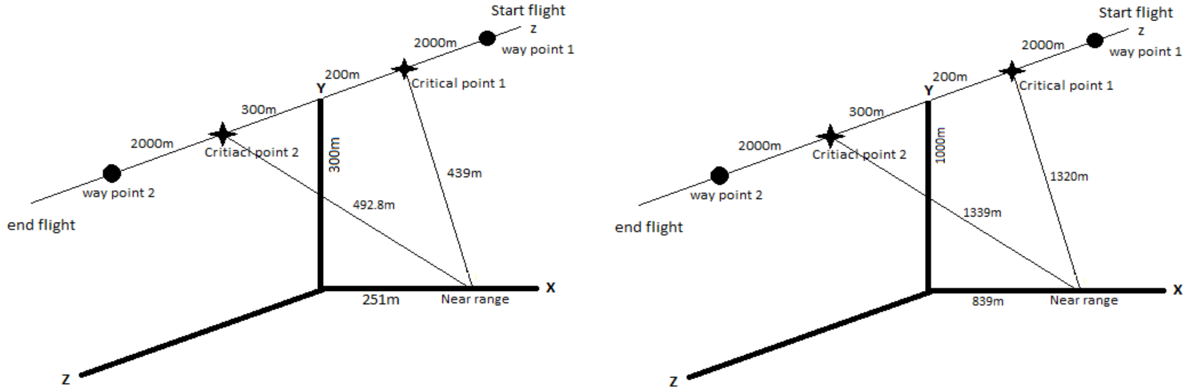

Figure 5.6: The aircraft track for the two flights where left is with 300m altitude and the right is 1000m altitude.

The value of incidence angle is calculated for the two flight altitude with three incidence angles for each altitude. The first incidence angle is for the near range which assumed to be 40^0, the second incidence angle for the mid-range, and the third incidence angle for the far range. The incidence angle increases from the near range to the far range. This can be observed in figure5.7 and 5.8 below with two different altitudes and presented in table 5.2.

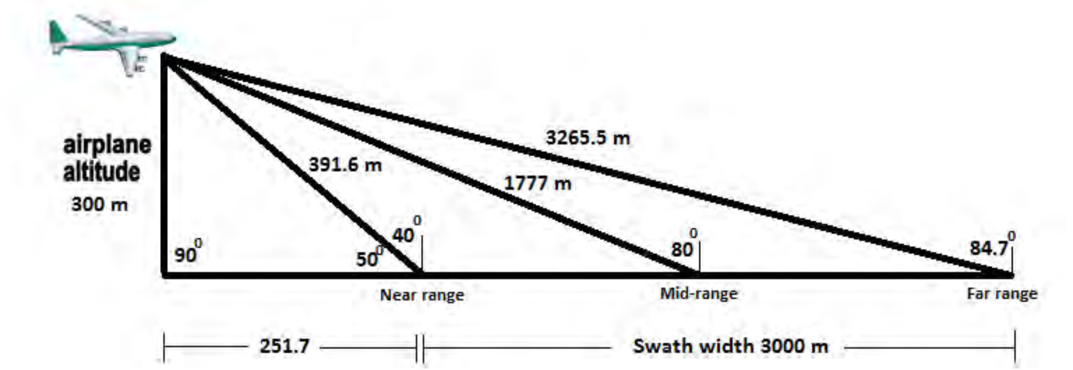

Figure 5.7: The incidence angles for the first flight with 300 m altitude.

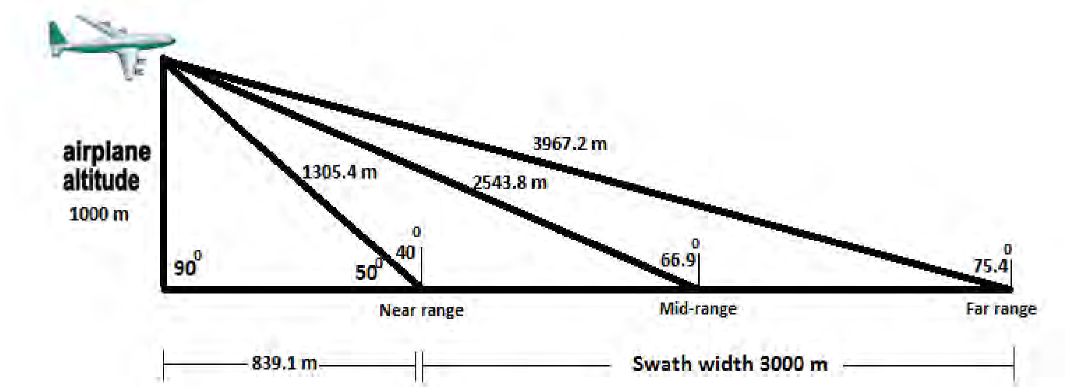

Figure 5.8: The incidence angles for the second flight with 1000 m altitude.

The calibration is achieved on the basis of the backscattered for both amplitudes and phase. The corner reflectors will help on calibrating the co-polarized channel as well as radiometric calibration. Global Positioning System (GPS) base stations will be used at the calibration site to deliver data for performing positional error correction for the *Cessna 208b*. This position calibration using data obtained from the Global Positioning System (GPS) station are referred as differential GPS (Differential Global Positioning System). The DGPS (Differential Global Positioning System) provides improved location accuracy, from the 15-meter nominal GPS accuracy to about 10 cm in case of the best implementations.

All the trihedral corner reflectors are setup to align the front horizontal edge of the corner reflector with the flight line and the boresight of the corner reflector aligned with the radar sensor. The reason is to maximize the signal return. Also, the elevation angle can be measured in setting the corner reflector. The elevation angle (θelv) is measured from the horizontal plane and the base surface of the corner reflector as shown in Figure 5.9. Therefore, the elevation angle is measured as follows:

$$(\theta elv = 90° - (\theta inc + \theta bore)). \tag{5.25}$$

The relation between elevation, bore-sight and incidence angle is shown in figure 5.9 below, where θbore is the inherent bore elevation of a corner reflector from horizontal, θinc is the desired incidence angle and θelv is the elevation angle.

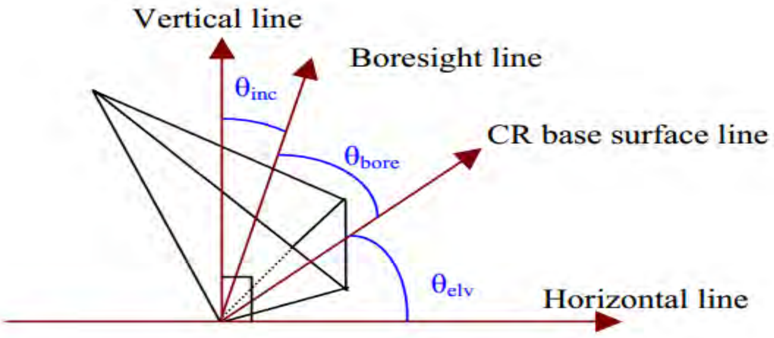

Figure 5.9: Relation between elevation, bore-sight and incidence angle [41]**.**

From table 5.2 which is the Incidence angles calculation for Waseda flights, we are going to deploy our trihedral corner reflectors based on elevation, bore-sight and incidence angles for the two flights. As shown in figure 3.2.B, the value of angle of incidence θ is 54.74^0 and ϕ equal to 45^0. The trihedral corner reflector will be supported by wood under the front edge. The front edge has to be parallel to the flight line. For example, the first incidence angle for the near range is 40^0 which is less than 54.74^0 , then we need to raise the bottom panel by a value that is equal to (54.74^0 - 40^0), which is 14.74^0. The 14.74^0 represents is the elevation angle θelv. The θbore angle is represented Figure 5.7 and 5.8 for the near range which is equal to 50^0. After calculating elevation and bore-sight angle for the mid and far ranges, the results are presented in table 5.2.

Table.5.2: The elevation, bore-sight, and incidence angle for the two flights

	Flight 300m			Flight 1000m		
	θinc	θbore	θelv	θinc	θbore	θelv
Near Range (2500m)	40^{0}	50^{0}	14.74^{0}	40^{0}	50^{0}	14.74^{0}
Mid-Range (4000m)	80^{0}	10^{0}	25.26^{0}	66.9^{0}	23.1^{0}	12.16^{0}
Far Range (5500m)	84.7^{0}	5.3^{0}	29.96^{0}	75.4^{0}	14.6^{0}	20.66^{0}

Finally, we want to set up the azimuth angle for all the reflectors in the near range, the mid-range and the far range. Figure 5.10 below is a map of our corner reflectors deployment in the field:

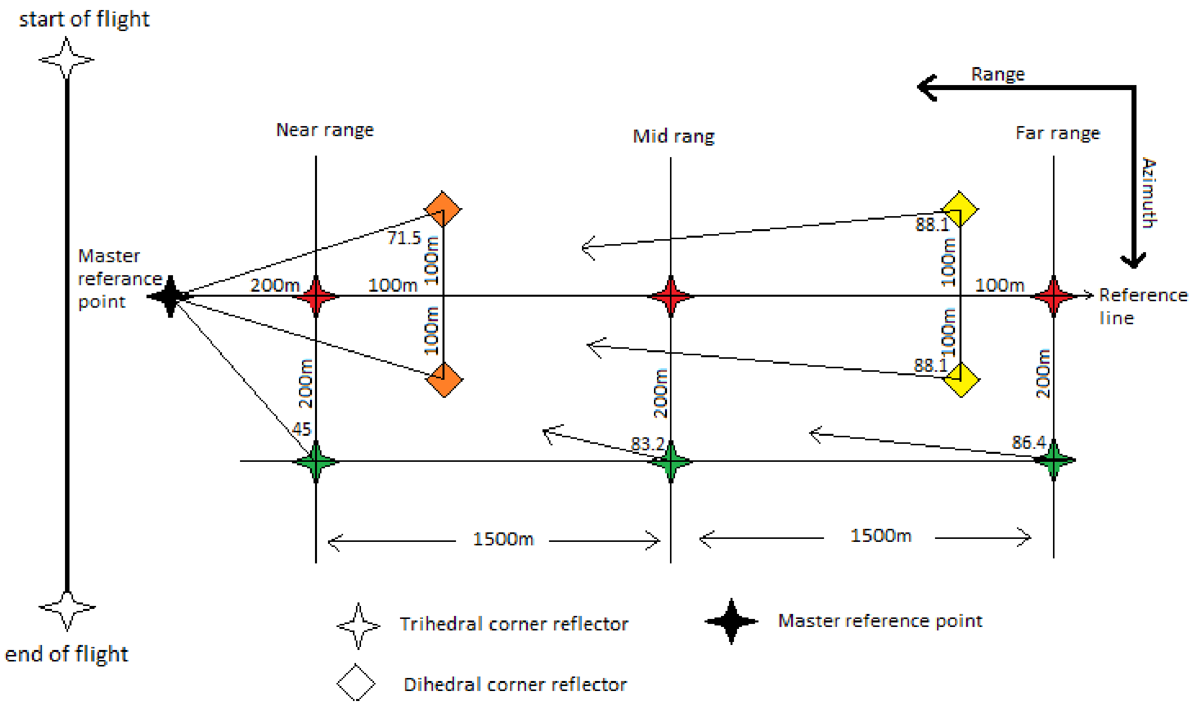

Figure 5.10: Deployment of corner reflectors on the field

The reflectors are going to be rotated in azimuth based on the master reference point in the above figure. The red trihedral corner reflectors will not be rotated because they are in the reference line and look direct to the master reference point. The green trihedral corner reflectors are 200m far from the reference line and they have to be rotated in azimuth to the right based on the angle to reference. The orange and yellow dihedral corner reflectors are 100m to the right and left from the reference line. The right dihedral corner reflectors have to be rotated to the left and the left dihedral corner reflectors have to be rotated to the right based on the angle to reference. Table 5.3 below shows the rotation angle for the reflectors which need to be rotated:

Table.5.3: the Rotated angle in azimuth to the angle of reference

	Rotated angle in azimuth to the angle of reference		
	Green trihedral corner reflectors	**Orange dihedral corner reflectors**	**Yellow dihedral corner reflectors**
Near range	45^0	18.5^0	No reflectors
Mid-range	6.71^0	No reflectors	No reflectors
Far range	3.6^0	No reflectors	1.9^0

In conclusion, the chapter concluded with a calibration procedure for the Waseda SAR sensor. The assumption which was made by Zebker and Lou, to calibrate the co-polarized phase, will be used in the calibration for Waseda. The reason for using Zebker and Lou assumption is because there's no calibration tone built into the radar system to accomplish the co-polarized channel imbalance. Also, the absolute radiometric calibration step will be done using Van Zyl theory because according to Van Zyl [19] even if we have a good knowledge of antenna gain patterns, as well as system parameters, the best way to accomplish the absolute radiometric calibration step is by placing corner reflectors to cover the image swath. The polarimetric response of each of the pixels containing a reflector will give us a polarization signature which we can compare to the ideal polarimetric reflector responses. Finally, the amplitude needs to be corrected after calibrating the phase. This step will be accomplished by measuring the power of the image, which came from the trihedral corner reflector, to correct co-polarized amplitude imbalance. The following chapter concludes the dissertation and gives a deduction of the results, as well as providing a way forward for future work and gives recommendations to be implemented in the future.

6

Conclusion and Future work

6.1. Conclusion

This dissertation provided knowledge and understanding synthetic aperture radar polarimetry from basic principle to an advanced calibration process. Various theorems of polarimetric decomposition were presented in the dissertation. Results show that the two coherent theorems, which are Pauli decomposition and Cameron decomposition, work better at detecting nature targets, while SDH is suitable for man-made targets. Also, Freeman decomposition from incoherent decomposition is suitable for detecting nature targets, while Yamaguchi decomposition work better with man-made targets.

The collected calibrated data from NASA's Uninhabited Aerial Vehicle Synthetic Aperture Radar (UAVSAR) over California were contaminated with an unrealistic high amount of coupling (-5 dB), to show the amount of coupling on the images for the three channels (HH, VV and HV). The amount of coupling for the HV channel is higher than the other two channels because -5dB from both HH and VV were added to HV. The vectors representation for one pixel proved our analysis by showing the pure value location and then the value of the vector after it is contaminated with -5 dB.

The developed calibration procedure will be used for calibrating the Waseda SAR sensor by estimation and removing the cross-talk parameters, using the development by Van Zyl, from the data itself. Also, Zebker and Lou's assumption is used for calibrating co-polarized channel imbalance by using external devices, which are trihedral corner reflectors. The overall radiometric calibration is done by replacing 6 trihedral corner reflectors and 4 dihedral corner reflectors. The first two trihedral corner reflectors, with different sizes for P-band and X-band, are placed close to the near range. The second two trihedral corner reflectors in the middle range and the last two trihedral reflectors are placed close to the far range. The dihedral corner reflectors are placed in the near and far range. The first two dihedral corner reflectors, with different sizes for P-band and X-band, are placed close to the near range and the last two dihedral reflectors are placed close to the far range.

The reason for using Zebker and Lou assumption is because there is no calibration tone built into the radar system to accomplish the co-polarized channel imbalance. Also, the absolute radiometric calibration step will be done using Van Zyl theory because according to Van Zyl [19] even if we have a good knowledge of antenna gain patterns, as well as system parameters, the best way to accomplish the absolute radiometric calibration step is by placing corner reflectors to cover the image swath.

6.2. Future Work

In this dissertation, we have proposed a calibration procedure of calibrating SAR images. The overall dissertation’s future work is summarized as follows:

- ***Un-calibrated Data:***

  Due to the difficulties in obtaining un-calibrated data, we can use the un-calibrated data, which will be obtained from Waseda SAR sensor, and apply the developed calibration procedure to test the results.

- ***Polarimetric Decomposition:***

  Polarimetric decomposition theorems are a powerful tool to extract the physical information from the target. These decomposition theorems will be used in future to analyze the Waseda sensor.

- ***Use of external devices for calibration:***

  The data, which was used in the dissertation, does not use any external devices, such as trihedral corner reflectors, that are deployed in the image. Having a trihedral corner reflector and dihedral corner reflector in the image is the best way to apply the developed calibration procedure. Six of the trihedral corner reflectors and dihedral corner reflectors can be deployed in the image to calibrate the data.

  The first two trihedral corner reflectors, with different sizes for P-band and X-band, are placed close to the near range. The second two trihedral corner reflectors in the middle range and the last two trihedral reflectors are placed close to the far range. The dihedral corner reflectors are placed in the near and far range. The first two dihedral corner reflectors, with different sizes for P-band and X-band, are placed close to the near range and the last two dihedral reflectors are placed close to the far range.

- ***Polarization signature:***

  The data in chapter five does not have any reflectors in the image. By having reflectors in the image, a polarization signature can be presented for one pixel and compared with the theory to remove any errors.

References

[1] A. Freeman, "Radiometric calibration of SAR image data," XVII Congress for Photogrammetry and Remote Sensing(ISPRS), 1992.

[2] T. A. Gardens. [Online]. Available: http://www.gibraltargardens.gi/PalmWeevil2.php. [Accessed 25 April 2015].

[3] J. Moreira, M. Schwäbisch, C. Wimmer, M. Rombach and J. Mura, "Surface and ground topography determination in tropical rainforest areas using airborne interferometric SAR," *Photogrammetric Week*, pp. 167-173, 2001.

[4] W. Boerner, Polarimetry in radar remote sensing. Basic and applied concepts, In manual of remote sensing: Principle and Applications of Imaging Radar, 3 ed., vol. 8, Wiley, 1998.

[5] J. Sen Lee and E. Pottier, Polarimetric Radar Imaging from basics to applications, NewYork: CRC Press, 2009.

[6] G. S. University, "HyperPhysics," [Online]. Available: http://hyperphysics.phy-astr.gsu.edu/hbase/phyopt/polclas.html. [Accessed 20 December 2014].

[7] C. C. f. R. Sensing, "Fundamentals of Remote Sensing Tutorial," Canada Center for Remote Sensing, [Online]. Available: http://www.nrcan.gc.ca/sites/www.nrcan.gc.ca/files/earthsciences/pdf/resource/tutor/fundam/pdf/fundamentals_e.pdf.

[8] Canada Center for Remote Sensing, "Basics of SAR Polarimetry," CCRS, 22 Novmber 2013. [Online]. Available: http://www.nrcan.gc.ca/earth-sciences/geomatics/satellite-imagery-air-photos/satellite-imagery-products/educational-resources/9575. [Accessed 25 July 2014].

[9] I. Woodhouse, Introduction to Microwave Remote Sensing, CRC Press, 2006.

[10] A. Andreou and Z. Kalayjian, "Polarization imaging: principles and integrated polarimeters," *Sensors Journal,IEEE* , vol. 2, no. 6, pp. 566-576, 2002.

[11] M. Borgeaud, "Theoretical Models for Polarimetric Microwave Remote Sensing of Earth Terrain," *Journal of Electromagnetic Waves and Applications*, vol. 3, no. 1, pp. 61-81, 1989.

[12] J. Richards, Remote Sensing with Imaging Radar, Springer, 2009.

[13] L. Zhang, J. Zhang, B. Zou and Y. Zhang, "Comparison of Methods for Target Detection and Applications Using Polarimetric SAR Image," *PIERS Online*, vol. 4, pp. 140-145, 2008.

[14] E. Krogager, W. Boerner and S. Madsen, "Feature-motivated Sinclair matrix (sphere/diplane/helix) decomposition and its application to target sorting for land feature classification," *Wideband Interferometric Sensing and Imaging Polarimetry*, vol. 3120, pp. 144-154, 1997.

[15] W. Cameron, N. Youssef and L. Leung, "Simulated Polarimetric Signatures of Primitive Geometrical Shapes," *IEEE Trans. on GRS*, vol. 34, no. 3, pp. 793-803, 1996.

[16] A. Freeman and S. Durden, "A Three-Component Scattering Model for Polarimetric SAR Data," *IEEE Transactions on Geoscience and Remote Sensing*, vol. 36, no. 3, pp. 963-973, 1998.

[17] Y. Yamaguchi, T. Moriyama, M. Ishido and H. Yamada, "Four-Component Scattering Model for Polarimetric SAR Image Decomposition," *IEEE Trans. On GRS*, vol. 43, no. 8, pp. 1699-1706, 2005.

[18] A. Freeman, "Radiometric Calibration of SAR Image Data," vol. 29, pp. 212-212, 1993.

[19] J. Van Zyl and Y. Kim, Synthetic Aperture Radar Polarimetry, New Jersey: Wiley, 2011.

[20] K. Sarabandi and T.-C. Chiu, "Optimum Corner Reflector For Calibration of Imaging Radars," vol. 44, no. 10, 1996.

[21] Y. Qin, D. Perissin and L. Lei, "The Design and Experiments on Corner Reflectors for Urban Ground Deformation Monitoring in Hong Kong," *International Journal of Antennas and Propagation*, p. 8, 2013.

[22] D. Brunfeldt and F. Ulaby, "Active Reflector for Radar Calibration," *IEEE Transactions on Geoscience and Remote Sensing*, Vols. GE-22, no. 2, pp. 156-169, 1984.

[23] H. Wakabayashi and S. Uratsuka, "Calibration and Data Comparison of Airborne L-band Polarimetric SAR," *Journal of the Remote Sensing Society of Japan*, vol. 24, pp. 64-74, 2004.

[24] X. Chen, T. Wu and X. Zhong, "Airborne polarimetric SAR experiments with different crosstalk calibration techniques," in *Radar , 2011 IEEE CIE International Conference*, Chengdu, 2011.

[25] J. van Zyl, "Calibration of Polarimetric Radar Images Using Only Image Parameters And Trihedral Corner Reflector Responses," vol. 28, no. 3, pp. 337 - 348 , 1990.

[26] Y.-L. Desnos and M. Loiselet, "ESR-1 and multifrequency polarimetric SAR calibration-validation results," *EARSeL advanced in remote sensing* , vol. 2, no. 2, pp. 22-32, 1993.

[27] S. Quegan, "A Unified Algorithm for Phase and Cross-Talk Calibration of Polarimetric Data-Theory and Observations," vol. 32, no. 1, pp. 89-99, 1994.

[28] H. Skriver, J. Dall and S. Madsen, "External polarimetric calibration of the Danish polarimetric C-band SAR," *Geoscience and Remote Sensing Symposium*, vol. 2, pp. 1105-1107, 1994.

[29] K. JEFFREY, "Calibration of complex polarimetric SAR imagery using backscatter correlations," *Aerospace and Electronic Systems, IEEE Transactions*, vol. 28, no. 1, pp. 183 - 194, 1992.

[30] T. Ainsworth and J. Lee, "A New Method for a posteriori Polarimetric SAR Calibration," in *Geoscience and Remote Sensing Symposium,Geoscience and Remote Sensing Symposium, 2001. IGARSS '01. IEEE 2001 International*, Sydney, 2001.

[31] A. G, B. D. Fore, B. P. Chapman and S. H. Hawkins, "UAVSAR Polarimetric Calibration," *Geoscience and Remote Sensing, IEEE Transactions on*, vol. 53, no. 6, pp. 3481 - 3491, 2015.

[32] L. Wuping and W. Chao, "COMPARISON OF POLARIMETRIC CALIBRATION TECHNIQUES AND THEIR," in *Geoscience and Remote Sensing Symposium (IGARSS), 2010 IEEE International*, Honolulu, HI, 2010.

[33] L. Liao, P. Li and J. Yang, "A MODIFIED METHOD FOR POLARIMETRIC SAR CALIBRATION ALGORITHM," *International Archives of the Photogrammetry, Remote Sensing and Spatial Information Sciences*, Vols. XL-7/W1, pp. 73-76, 2013.

[34] Y. Lou and J. van Zyl, "Relative phase calibration of the NASA/DC-8 three-frequency polarimetric SAR system," in *Geoscience and Remote Sensing Symposium, 1992. IGARSS '92. International*, Houston,USA, 1992.

[35] Z. Howard and Y. Lou, "Phase Calibration of Imaging Radar Polarimeter Stokes Matrices," *IEEE Geoscience and Remote Sensing Society*, vol. 28, no. 2, pp. 246 - 252, 1990.

[36] J. vanZyl and H. A. Zebker, Imaging Radar Polarimetry, 1993.

[37] "Modeling and Observation of the Radar Polarization Signature of Forested Areas," vol. 27, no. 3, pp. 290-301, 1989.

[38] NASA, "http://uavsar.jpl.nasa.gov/," jet propulsion laboratory , 2014. [Online]. [Accessed 5 January 2015].

[39] p. s. MetaSensing BV, "NESZ plots for X band, P band for Waseda SAR," Metasensing, Netherland, 2015.

[40] C. Wolff, "Radar Tutorial," [Online]. Available: http://www.radartutorial.eu/20.airborne/ab06.en.html. [Accessed April 2015].

[41] C. Liu, N. Sandirasegaram and R. A., "MarCoPola Polarimetric SAR Trial:Signatures of Multiple Vessels with Aligned Operating Conditions," Defence R&D Canada, Ottawa , September 2005.

[42] J. Van Zyl and Y. Kim, Synthetic Aperture Radar Polarimetry, New Jersey: John Wiley & Sons,Inc, 2011.

[43] P. Churchill and E. Attema, "The European Airborne Polarimetric SAR Campagn MAESTRO 1," Finland, Jan 1990.

[44] F. Henderson and A. Lewis, Principles & Applications of Imaging Radar, Manual of Remote Sensing, 3 ed., John Wiley & Sons, Inc, 1998.

[45] K. Sarabandi, F. Ulaby and A. Tassoudji, "Calibration of Polarimetric Radar Systems With Good Polarization Isolation," vol. 28, no. 1, pp. 70-75, 1990.

Appendix A-1

```
x=interpol([-45,45],91)
y=interpol([0,180],91)
xx=(x/180)*!pi
yy=(y/180)*!pi
xlen=n_elements(xx)
ylen=n_elements(yy)
xmesh=replicate(1,ylen)##xx
ymesh=rebin(reform(yy,1,ylen),xlen,ylen)
z=1- cos(4*xmesh)
isurface,z,x,y,XRange=[-45, 45], YRange=[0, 180], $
  ZRANGE=[0, 2],YSTYLE=2.5, ZSTYLE=2.5, CHARSIZE=2.5,$
  TITLE='Trihedral Corner Reflector',XTITLE='Ellipticity Angle (Degree)',
YTITLE='Orientation Angle (Degree)'
End
```

Appendix A-2

```
x=interpol([-45,45],91)
y=interpol([0,180],91)
xx=(x/180)*!pi
yy=(y/180)*!pi
xlen=n_elements(xx)
ylen=n_elements(yy)
xmesh=replicate(1,ylen)##xx
ymesh=rebin(reform(yy,1,ylen),xlen,ylen)
z=1+ cos(4*xmesh)
isurface,z,x,y,XRange=[-45, 45], YRange=[0, 180], $
  ZRANGE=[0, 2],YSTYLE=2.5, ZSTYLE=2.5, CHARSIZE=2.5,$
  TITLE='Trihedral Corner Reflector',XTITLE='Ellipticity Angle (Degree)',
YTITLE='Orientation Angle (Degree)'
End
```

Appendix B-1

```
x=interpol([-45,45],91)
y=interpol([0,180],91)
xx=(x/180)*!pi
yy=(y/180)*!pi
xlen=n_elements(xx)
ylen=n_elements(yy)
xmesh=replicate(1,ylen)##xx
ymesh=rebin(reform(yy,1,ylen),xlen,ylen)
z=1-(cos(2*xmesh)^2)*(cos(4*ymesh))-(sin(2*xmesh)^2)
isurface,z,x,y,XRange=[-45, 45], YRange=[0, 180], $
  ZRANGE=[0, 2],YSTYLE=2.5, ZSTYLE=2.5, CHARSIZE=2.5,$
  TITLE='Drihedral Corner Reflector',XTITLE='Ellipticity Angle (Degree)',
YTITLE='Orientation Angle (Degree)'
End
```

Appendix B-2

```
x=interpol([-45,45],91)
y=interpol([0,180],91)
xx=(x/180)*!pi
yy=(y/180)*!pi
xlen=n_elements(xx)
ylen=n_elements(yy)
xmesh=replicate(1,ylen)##xx
ymesh=rebin(reform(yy,1,ylen),xlen,ylen)
z=1+(cos(2*xmesh)^2)*(cos(4*ymesh))+(sin(2*xmesh)^2)
isurface,z,x,y,XRange=[-45, 45], YRange=[0, 180], $
  ZRANGE=[0, 2],YSTYLE=2.5, ZSTYLE=2.5, CHARSIZE=2.5,$
  TITLE='Drihedral Corner Reflector',XTITLE='Ellipticity Angle (Degree)',
YTITLE='Orientation Angle (Degree)'
End
```